Lithospheric Structure of Africa and Surrounding Regions Revealed by Earthquake and Ambient Noise Surface Wave Tomography

Adebayo Oluwaseun Ojo[1,4], Weisen Shen[2], Sidao Ni[3], Li Zhao[1], Jun Xie[3], Honn Kao[4,5]

[1]School of Earth and Space Sciences, Peking University, Beijing, 100871, China
[2]Department of Geosciences, State University of New York at Stony Brook, Stony Brook, NY, USA
[3]State Key Laboratory of Geodesy and Earth's Dynamics Institute of Geodesy and Geophysics, CAS
[4]Geological Survey of Canada, Natural Resources Canada, Sidney, British Columbia, Canada
[5]School of Earth and Ocean Science, University of Victoria, Victoria, British Columbia, Canada

Abstract

To advance the understanding of the tectonic processes shaping the African continent, we construct the first continental-scale shear-wave velocity (Vs) model of the crust and uppermost mantle from joint analysis of ambient seismic noise and earthquake data recorded by ~1529 broadband seismic stations located in Africa, Arabia, and Europe from 1987 to 2018. We apply the widely used ambient noise cross-correlation and earthquake two-station methods to retrieve the fundamental-mode Rayleigh-wave group and phase velocity dispersions in the period range of 5 – 50 s which are jointly inverted using the neighbourhood algorithm to build a new three-dimensional Vs model with associated uncertainties. The inclusion of relatively short-period dispersion data from ambient seismic noise allows us to achieve better resolution at shallow depth and obtain a more accurate model than previous global and continental-scale studies, revealing lithospheric structures that correlate well with known tectonic features. In sparsely instrumented regions of north-central Africa, our model provides seismic evidence for the existence of cratonic remnants beneath thick sediments within the poorly imaged Sahara Metacraton and reveals unique mantle upwelling beneath hotspots, suggesting that they may be fed by unconnected plumes. The estimated crustal thickness varies among and within tectonic provinces and shows no clear evidence for the secular variation in crustal genesis. Our new model has the potential to serve as a preliminary reference velocity model for Africa and is useful for practical applications, including monitoring of the Comprehensive Nuclear-Test-Ban Treaty, geodynamic modeling as well as seismic hazard analysis.

1 Introduction

The continent of Africa contains several important tectonic features with records that span well over 3.7 Ga of earth's history (Milesi et al., 2010). These include Archean Cratons, Proterozoic mobile belts, Mesozoic and Cenozoic rifts and hotspots, large sedimentary basins, and widespread Precambrian crust that have been shaped by several past and ongoing tectonic processes (Begg et al., 2009). Surrounding the continent are divergent plate boundaries and passive continental margins resulting from the Mesozoic breakup of Gondwana and the opening of the Atlantic Ocean (Ebinger, 2005; Fishwick & Bastow, 2011; Tugume et al., 2013; Figure 1). The scientific curiosity to understand the origin and evolution of these

prominent geological features in Africa led to the deployment of a growing number of seismic networks, e.g., the Africa-Array (Durrheim, 2008; Nyblade et al. 2008; Durrheim & Nyblade, 2019), SASE (Yang et al., 2008), CBSE (Tokam et al., 2010), etc. in and around the African continent in the past few decades.

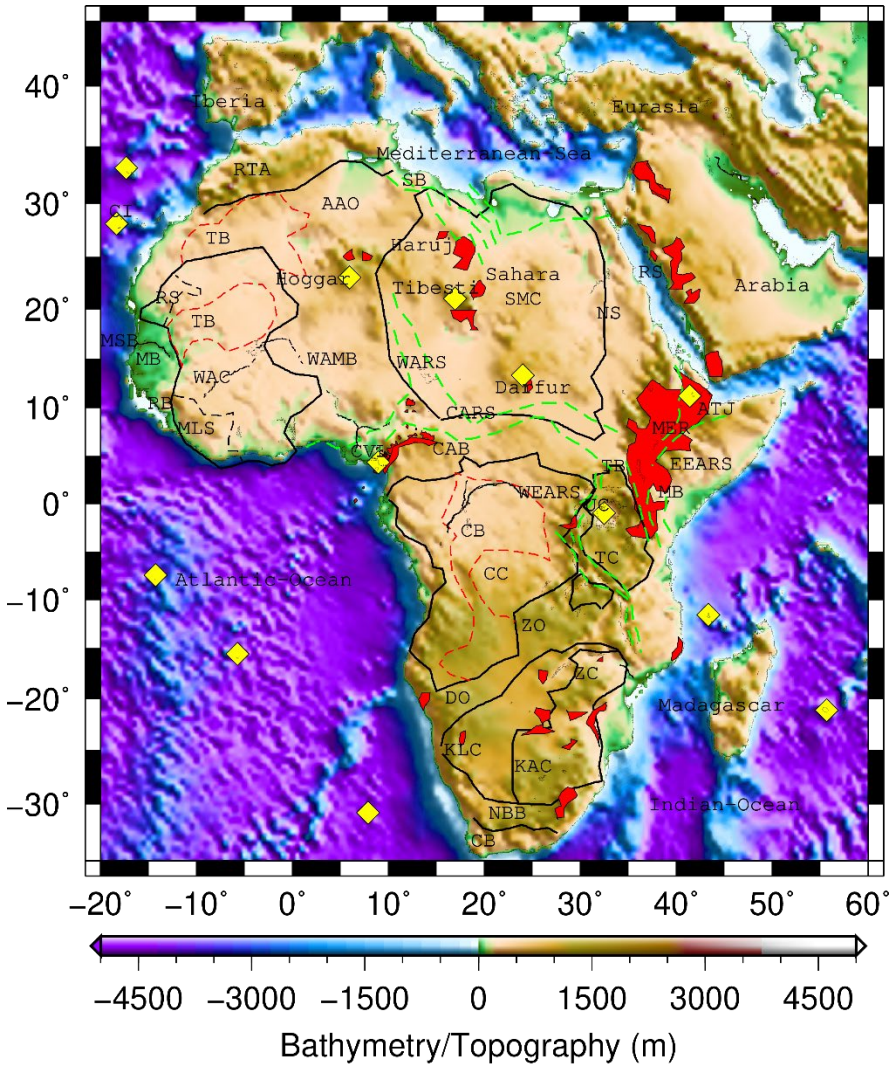

Figure 1. Map of the study area showing the main tectonic features (modified after Globig et al., 2016) overlain on the bathymetry and topography derived from ETOPO1 (Amante & Eakins, 2009). Denoted on the map are the locations of the tectonic features in and around the African continent including CPB (Cape Belt), NNB (Namaqual-Natal Belt), KLC (Kalahari Craton), KAC (Kaapvaal Craton), ZBC (Zimbabwe Craton), DMO (Damara Orogen), ZBO (Zambezi Orogen), CGC (Congo Craton), CGB (Congo Basin), TZC (Tanzania Craton), UGC (Uganda Craton), WEARS (Western East African Rift System), EEARS (Eastern East African Rift System), TKB (Turkana Basin), MZB (Mozambique Belt), MER (Main Ethiopian-Rift), ATJ (Afar Triple Junction), CVL (Cameroon Volcanic Line), CAB (Central African Belt),

CARS (Central African Rift System), WAC (West African Craton), WAMB (West African Mobile Belt), NBS (Nubia Shield), RS (Red Sea), SRB (Sirt Basin), MLS (Man-Leo Shield), TDB (Taoudeni Basin), RKB (Rockellides Belt), MTB (Mauritanian Belt), MSB (Mauritanian-Senegal Basin), RGS (Reguibat Shield), CNI (Canary Island); RTA (Rif-Tell-Atlas Mountain); AAO (Anti-Atlas Orogen), SMC (Saharan Metacraton). Red patches and yellow diamonds show locations of Cenozoic volcanism and hotspots, respectively. Green dashed lines mark zones of continental rifting and red dashed lines define boundaries of intra-cratonic basins.

Data from these deployments have been used in a lot of studies that provided us with a fundamental understanding of the structure, composition, and geodynamic evolution of these tectonic features (e.g., Adams et al., 2018; Accardo et al., 2020; Celli et al., 2020; Chambers et al., 2019; Ebinger et al., 2019; Hassan et al., 2020; Hopper et al., 2020; Kachingwe et al., 2015; Ojo et al., 2018, 2019; Sobh et al., 2020; Wang et al., 2019 and references therein). However, these studies are either small-scale local or large-scale global studies that do not sufficiently address the regional-scale lateral and depth variations of the lithospheric structure of the entire African landmass. A cross-evaluation of the existing models from small-scale studies across the continent published by different authors is not straightforward as they came from different datasets with varying measurement uncertainties, non-uniform processing techniques, and resolutions in addition to the use of a variety of methods. Our current understanding of the continental-scale lithospheric structure of Africa and the relationship between the various tectonic provinces primarily came from global models that cover this continent, however, they usually bear worse resolution and not capable to address specific scientific problems of interest (e.g., Woodhouse & Dziewonski, 1984; Cadek & Martinec, 1991; Trampert & Woodhouse, 1995; Nataf & Richard, 1996; Mooney et al., 1998; Ritsema et al., 1999; Boschi & Ekstrom, 2002; Grand, 2002; Ritzwoller et al., 2002; Shapiro & Ritzwoller, 2002; Zhou et al., 2006; Meier et al., 2007; Lebedev et al., 2009; Pasyanos et al., 2014; Rychert & Shearer, 2009; Laske et al., 2013; Schaeffer & Lebedev, 2013). This is primarily attributed to a lack of data in several parts of the continent inhibiting their ability to achieve a satisfactory resolution to targeted structures. The majority of existing broadband seismic stations are located in the southern and eastern parts of the continent, therefore, a good portion of the continent (e.g., Central, Northern and Western parts) remains poorly constrained seismologically due to the lack of densely and uniformly distributed stations in addition to low seismicity (Van der Meijde et al., 2015; Figure 2). To the best of our knowledge, only a limited number of studies have attempted to develop a regional-scale model of Africa from seismic and/or gravity data (e.g., Sebai et al., 2006; Pasyanos & Nyblade, 2007; Priestley et al., 2008; Begg et al., 2009; Fishwick, 2010; Tedla et al., 2011; Laske et al, 2013; Tugume et al., 2013; Pasyanos et al, 2014; Globig et al., 2016; Celli et al., 2020). More so, these previous regional-scale studies on the continent focused more on the upper mantle structure while ignoring or correcting for crustal effects, leaving fundamental questions regarding

the crustal structure unresolved (e.g., Deen et al., 2006; Ritsema & van Heijst, 2000; King & Ritsema, 2000; Lekic et al., 2010; Panning et al., 2010; Beggs et al., 2009; Adams et al., 2012; Emry et al., 2019).

A more comprehensive understanding of the regional tectonics of Africa necessitates the development of a robust continent-wide seismic model from detailed imaging of both shallow and deep structures across the continent using the same methodology and data processing procedure. An effective approach to solving the current situation of uneven data coverage and achieving this goal would be to densify the seismic stations across the African continent as we have in other more developed parts of the world, such as the USArray and Hi-net programs. However, this is an expensive approach with economic constraints and other challenges. In this study, we adopt a proactive approach to mitigating this problem and develop a new seismic model of the African lithosphere that provides significant improvements over previous continental-scale studies. For the first time, we combine dispersion data obtained from cross-correlations of ambient seismic noise and earthquake records to image the entire African continent similar to other successful studies (e.g., Yao et al., 2008; Yang et al., 2008a,b; Yang & Ritzwoller, 2008; Lebedev et al., 2009; Moschetti et al., 2010; Yoshizawa & Ekstrom, 2010; Endrun et al., 2011; Zhou et al., 2012; Agius & Lebedev, 2013; Shen et al., 2013; Huang et al., 2014; Chen et al., 2014; Pourpoint et al., 2018; Ojo et al., 2018). This enables us to obtain up to 50,000 inter-station ray paths crisscrossing the entire continent at an unprecedented density, thereby improving the spatial resolution in sparsely instrumented regions in Africa and achieve sensitivity to both shallow and relatively deep lithospheric structures (e.g., Kastle et al., 2018; Pourpoint et al., 2018). This paper discusses this effort by first providing a summary of the tectonic settings in the study area in Section 2, showing the data and method in Section 3, and then presenting the results and interpretation in Section 4. We also provide a detailed discussion on specific scientific questions in Section 5 and summarize the paper in Section 6.

2. Tectonic and Geological Configuration of the Study Area

In this section, we provide a sufficient description of the most remarkable geologic features in the Eastern, Western, Southern, and Northern part of the continent as a guide to the interpretation of the shear-wave velocity model developed in this study. However, we acknowledge that it is outside the scope of this paper to present a detailed tectonic evolution of the African continent and refer readers to Begg et al. (2009) and references therein for a more complete description of the African geology and tectonics.

2.1 Eastern Africa

The region of eastern Africa has been the attention of a lot of studies primarily because of the ongoing continental rifting along the boundary between the Nubia and Somalia plates, marked by the 5000 km long East African Rift System (EARS) which is active both seismically and volcanically (McConnell, 1972;

Chorowicz, 2005). This divergent plate boundary extends from eastern to southern Africa and preferentially splits into two distinct branches (i.e. the eastern EARS and the western EARS) in the center around the Archean Tanzania Craton (TZC, see Figure 1). Although the western EARS is seismically active and characterized by a few isolated regions of magmatism, the eastern EARS is characterized by widespread magmatism (Ebinger, 1989). The EARS exhibit different stages and styles of continental rift development that is most likely enhanced by magmatic processes in the upper mantle (e.g., Nyblade & Robinson, 1994; Bagley & Nyblade, 2013; Ring, 2004). Its geodynamic origin and evolution are hotly debated in literature with proposed mechanisms ranging from single to multiple plumes and possible connection to the African Superplume (e.g., Nyblade & Robinson, 1994; Grand et al., 1997; Ebinger & Sleep, 1998; George et al., 1998; Lithgow-Bertelloni and Silver, 1998; Ritsema et al., 1998, 1999; Gurnis et al., 2000; Rogers et al., 2000; Furman et al., 2004; Kieffer et al., 2004; Benoit et al., 2006; Pik et al., 2006; Simmons et al., 2007; Bastow et al., 2008; Forte et al., 2010; Hilton et al., 2011; Hansen & Nyblade, 2013).

The Red Sea and Gulf of Aden rifts began forming in the Oligocene when Arabia first separated from Africa. Together with the East African Rift, they form a triple junction in the Afar depression (Begg et al., 2009). The Main Ethiopian Rift (MER) is in the northern part of the EARS where magma-assisted continental rifting started about 31–29 Ma and transitions into incipient seafloor spreading in Afar depression (Wolfenden et al., 2004; Bosworth et al., 2005). The MER transects the Ethiopian Plateau, a 1000 km wide Palaeogene flood basalt province uplifted to an elevation of ~2.5 km after the impingement of the Afar mantle plume at the base of the lithosphere around ~30 Ma (Ebinger & Sleep, 1998). The magma-poor and weakly extended Malawi rift zone is about 800 km long beginning from the Rungwe Volcanic Province in the north to the Urema Graben in the south and mainly occupied by Lake Malawi which consists of several half-grabens bounded by border faults (e.g., Ebinger et al., 1989; Jackson & Blenkinsop, 1993; Craig et al., 2011; Fagereng, 2013; Laó-Dávila et al., 2015).

The Uganda and Tanzania Cratons are both located between the western and eastern branches of EARS. The Achaean TZC forms the nucleus of the Precambrian tectonic framework of eastern Africa and is surrounded by several Proterozoic mobile belts which are shaped primarily by the process of obduction (Cahen et al., 1984). The dominant rock types that make up the TZC are granitoid and gneisses formed about 2.7-2.5 Ga and the Palaeoproterozoic Rwenzori Fold Belt in the northwest consisting mainly of metasedimentary rocks intercalated by granitoid (Cahen et al., 1984; Schulter, 1997; Manya & Maboko, 2003; Begg et al., 2009). The Uganda Craton lies to the north of the TZC and contains Neoproterozoic units that overlie its northeastern boundary with the Congo Craton in southwestern Africa. During the last 80 Ma, the craton has been affected by kimberlite volcanism (Chesler, 2012).

2.2 Northern Africa

The northward movement of the relatively stable African continent (~2–6 mm/yr) and its subsequent collision with the Eurasian plate starting from ~40 Ma led to the closure of the Tethys Ocean and the formation of tectonically complex northern and northwestern margins of the African plate (e.g., Abdelsalam et al., 2002, 2011). This also led to the formation, beginning from Cenozoic till today, of the Rif-Tell-Atlas Orogenic system, an intra-continental mountain belt marked by high topography (~2000 m) extending over 2000 km from Morocco to Tunisia (see Figure 1). Although the geodynamic evolution of the Rif-Tell Mountains of the Atlas System is highly debatable, it is suspected to result from the closure of the Tethys Ocean by subduction in the Western Mediterranean and further slab retreat (e.g., Vergés & Sàbat, 1999; Faccenna et al., 2004; Rosenbaum & Lister, 2004). The northward movement of the African plate and its convergence with the Eurasian plate also complicates the geology of the Mediterranean region in southern Europe (Faccenna et al., 2001; Lu et al., 2018; Manu-Marfo et al., 2019). The region is marked by subductions and collision of several microplates sandwiched between the larger tectonic plates. Similarly, several Triassic and Jurassic rifting episodes created basins (e.g., the Central African Rift System) along the inherited zones of crustal weakness in combination with the opening of the Atlantic Ocean (e.g., Frizon de Lamotte et al., 2000).

Eocene to Quaternary hotspot volcanic centers marked by topographic swells are also found in northern Africa. They are Hoggar in southern Algeria, Tibesti in northern Chad, and Darfour in western Sudan (Brown & Girdler, 1980; Nocquet & Calais, 2003; McClusky et al., 2003; Rosenbaum & Lister, 2004). Investigations of the magmatic plumbing system beneath these alkaline volcanoes suggest the existence of a unique plume source beneath all the volcanic centers or the migration of plumes from the Afar depression (Wilson & Guiraud, 1992; Burke, 1996; Ebinger & Sleep, 1998). Additionally, the upwelling of plumes due to small-scale mantle convection induced by the Africa-Eurasia collision may also be responsible for feeding the volcanic centers (Bailey, 1992).

Also in northern Africa is the enigmatic Saharan Metacraton which underlies much of the Sahara desert region between the West African Mobile Zone and the Arabian-Nubian Shield (Schandelmeier et al., 1994; Abdelsalam et al., 2002). The pre-Neoproterozoic character of its cratonic fragments indicates that it has been reworked by later Neoproterozoic collision events which most likely led to the delamination and/or basal erosion of the cratonic lithosphere (Abdelsalam et al., 2002; Lucassen et al., 2008; Begg et al., 2009; Shang et al., 2010; Fezaa et al., 2010; Abdelsalam et al., 2011). Likewise, the presence of scattered Precambrian outcrops in the region possibly indicates the existence of cratonic bodies underneath the thick Phanerozoic sediments in the Sahara desert (Condie, 1982).

Adjacent to the African plate in the northeast is the Arabian plate characterized by the Arabian shield near the Red Sea and Arabian Platform towards the eastern part of the plate. The plate is covered by sediments that thickens towards the east from the shield to the Mesopotamian Foredeep and Persian Gulf

(Seber et al., 1997; Tang et al., 2016; Yao et al., 2017; Kaviani et al., 2020). Expressions of widespread Cenozoic volcanism are also found within the plate.

2.3 Southern Africa

The region of southern Africa is characterized by anomalously high elevations compared to the global continental average elevation and contains the world's oldest Archean cratons (i.e. the Zimbabwe and Kaapvaal cratons) sandwiched between Orogenic belts. It also hosts two renowned igneous provinces, the Okavango dyke swarm and Bushveld mafic intrusion, formed between 2.7 and 0.3 Ga (de Wit et al., 1992; Nyblade & Robinson, 1994; Jelsma & Dirks, 2002). The Kaapvaal craton combines several terranes which consist mainly of granite-greenstone with narrow greenstone belts formed between 3.7 and 2.7 Ga and subsequently affected by several tectono-thermal events (De Wit et al., 1992; Eglington & Armstrong, 2004; Johnson et al., 2006; Begg et al., 2009). Similarly, the Zimbabwe craton formed between 3.6 and 2.5 Ga. The craton is underlain by the Paleoarchean lithosphere, suggesting that the isolation from the convective mantle most likely occurred during the initial phase of craton formation. The last tectono-thermal event that affected the craton occurred during the emplacement of the Great Dike around 2.58 Ga (Jelsma & Dirks, 2002). The Zimbabwe and Kaapvaal cratons are separated by the east-west trending Limpopo orogenic belt resulted from the collision between the two cratons around 2.7 Ga. The Limpopo orogenic belt consists of highly metamorphosed granite-greenstone and granulite terrains, which underwent a series of orogenic events between 2.0 and 3.0 Ga (McCourt & Armstrong, 1998; Kramers et al., 2006). Located in the southernmost end of the region is the Cape Fold Belt (0.3 Ga) formed during a younger orogenic event in the late Proterozoic/early Cambrian Saldanian Orogeny and the late-Paleozoic Cape Orogeny (Rozendaal et al., 1999). The youngest tectonic province in the region is the Namaqua-Natal mobile belt which was joined with the Kaapvaal Craton during the Namaqua Orogeny between 1.3 and 1.0 Ga. A large proportion of the belt has been covered by Phanerozoic sediments with a few surface exposures in the eastern Natal and the western Namaqua sectors (Thomas et al., 1989; Cornell et al., 2006).

Off the southeastern shore of Africa lies Madagascar that drifted south-southeasterly away from Africa along with India about 165–130 Ma during the break-up of Gondwana (Rabinowitz et al., 1983; Coffin & Rabinowitz, 1987; Kusky et al., 2007). This led to the opening of the Mozambique Channel and the formation of the Somali and the Mozambique oceanic basins (Rabinowitz et al., 1983; Piqué, 1999). Similarly, the rifting thinned the crust along the west coast of Madagascar, allowing Late Carboniferous to Quaternary age sedimentary basins, such as the Antsiranana, Mahajanga, and Morondava rift basins, to form on top of the Karoo sequence. This also led to the emplacement of volcanic rocks that have been reworked during the Pan-African Orogeny across many regions of Madagascar (e.g. Rabinowitz et al., 1983; Coffin & Rabinowitz, 1987; Nicollet, 1990; Storey et al., 1995; Torsvik et al., 1998; de Wit, 2003;

Collins, 2006; Pratt et al., 2017). The widespread flood basalts with surface exposure along the periphery of the island are commonly linked to the migration of Madagascar/India over the Marion hotspot (Storey et al., 1995; Torsvik et al., 1998). Subsequent rifting of the Indian subcontinent along a transform fault from 95 Ma to 84 Ma further shaped the east coast of Madagascar (e.g., Nicollet, 1990; de Wit, 2003). Since then, the entire island has remained tectonically stable.

2.4 Western Africa

The geology of western Africa is characterized by the Archean West African Craton (WAC) which contains a mechanically weak intra-cratonic depression in the center playing host to the Taoudeni Basin filled with ~3 km of Neoproterozoic to Paleozoic deposits alongside two other sedimentary basins, the Tindouf and Volta basins, and major shield bodies, the Reguibat and Man shields (MacGregor et al., 1998; Figure 1). Sedimentation in the basins began in late Proterozoic and continued well into Phanerozoic (Petters, 1991). Several Pan-African and Hercynian belts surround the WAC along the eastern (the Pharusian and Dahomeyides belts), western (the Rokellides and Mauritanides belts) and northern (Anti-Atlas belt) margins. The WAC and the Saharan Metacraton to the north are separated by the West African Mobile Zone (WAMZ), a typical configuration observed around Archean cratons in different parts of the continent. The Archean to Paleoproterozoic Congo Craton occupies most of the landmass in the southern part of western Africa and is surrounded by Pan-African foreland belts. The craton consists of granites and gneisses intruded by magmatic rocks that have been altered to form the greenstone belts which were subsequently intruded by granodiorites at about 2.9 Ga (Cahen et al., 1984; Tchameni et al., 2001; Begg et al., 2009; Tadjou et al., 2009). The craton also contains an intracontinental depression which is largely covered by the Proterozoic Congo Basin filled with about 4–9 km of Proterozoic to Neogene sediments with very slow subsidence since the Pan-African event (Crosby et al., 2010; Kadima et al., 2011). A large portion of western Africa experienced flood magmatism at about 137–127 Ma when the south Atlantic opened (e.g., Turner et al., 1994). The Mesozoic rifting and break-up of Gondwana led to the development of the Central African Rift System and the widespread extensional basins from Somalia to South Africa (e.g., Veevers et al., 1994; Burke, 1996).

The Cameroon Volcanic Line (CVL) is a linear chain of volcanoes of about 1600 km long traversing both the ocean (Gulf of Guinea) and the continent in Cameroon, western Africa. CVL comprises of 10-15 volcanic centers without age progression, a characteristic that makes it enigmatic. Volcanism commenced at 42 Ma in the continental sector and 30 Ma in the oceanic sector, and the volcanic rocks in both the oceanic and continental sectors are predominantly alkaline basalts (Fitton & Dunlop, 1985). The origin of the Eocene to Recent alkaline volcanoes is mostly thought to be small-scale mantle convection driven by several phenomena (e.g., King & Anderson, 1995, 1998; King & Ritsema, 2000; King, 2007; Adams et al.,

2018; Ojo et al., 2018). Mount Cameroon is considered the only active volcano with the most recent eruption in 2000 (Tokam et al., 2010).

The Central African Shear Zone (CASZ) within the Oubanguides mobile belt formed during the amalgamation of Gondwana and represents the ENE-WSW Precambrian lineament stretching from the Darfur region of Sudan into central Cameroon and disappearing beneath the Oligocene and younger volcanic materials at the southwest end of the CVL. The CASZ is thought to be an extension of the Pernambuco fault in Brazil (Dorbath et al., 1986). To the south of the CVL is the Benue Trough, a failed triple rift junction in Nigeria. Rifting in the Benue Trough started about 140 Ma and continued during the opening of the equatorial Atlantic (119-105 Ma) up until 84 Ma when it underwent a brief period of compression (Fairhead, 1988; Maluski et al., 1995). The Benue Trough was formed in the Proterozoic mobile belts surrounding the Archean Congo Craton and characterized by volcanism between 74-49 Ma (Maluski et al., 1995).

3 Data and Methodology

3.1 Ambient Seismic Noise and Earthquake Data

For this study, continuous ambient seismic noise and earthquake data recorded by 1529 broadband seismic stations belonging to 73 permanent and temporary seismic networks deployed in Africa, Europe, and Arabia over the past three decades are downloaded from the Incorporated Research Institutions for Seismology Data Management Center (IRIS-DMC). Figure 2 shows the distributions of stations and earthquakes. We retrieve daily ambient seismic noise records on the vertical component with a sampling frequency of 1 Hz for the entire lifespan of a station or up until mid-2018. We also retrieve data from earthquakes of $M_W \geq 5.0$ with epicentral distances of 30°-120° and depths shallower than 100 km from 1978 to 2018.

3.2 Rayleigh Waves from Ambient Noise Cross Correlations and Earthquakes

The data processing procedures to extract fundamental mode Rayleigh waves from ambient seismic noise and earthquake records are well known and fully described in our earlier papers (Ojo et al., 2017, 2018). Here, we provide a brief description of the parameters we employed in this study. We begin with removing the mean, linear trend, and instrument response from the daily ambient noise records, then apply a Butterworth band-pass filter in periods of 5–50 s before partitioning the data into one-hour segments for computational efficiency (e.g., Li et al., 2009). Similar to Bensen et al. (2007), we performed time-domain normalization using the running-absolute-mean method to reduce the influence of earthquakes as well as persistent monochromatic noises (e.g., Xia et al., 2013, 2020; Zeng and Ni, 2011), and a frequency domain whitening over the frequency band of 0.025–0.2 Hz to broaden the frequency spectrum of the ambient noise data and balance the energy. The resulting one-hour-long traces are cross-correlated between all the station

pairs with overlapping operation times and then stacked with their time-reversed cross-correlograms to obtain the symmetrical noise correlation function (NCF). This enhances the Rayleigh-wave signal by suppressing errors due to uneven distributions of the noise field. Finally, we stack all the available cross-correlations for a given station pair to produce the final NCFs used for subsequent dispersion analysis.

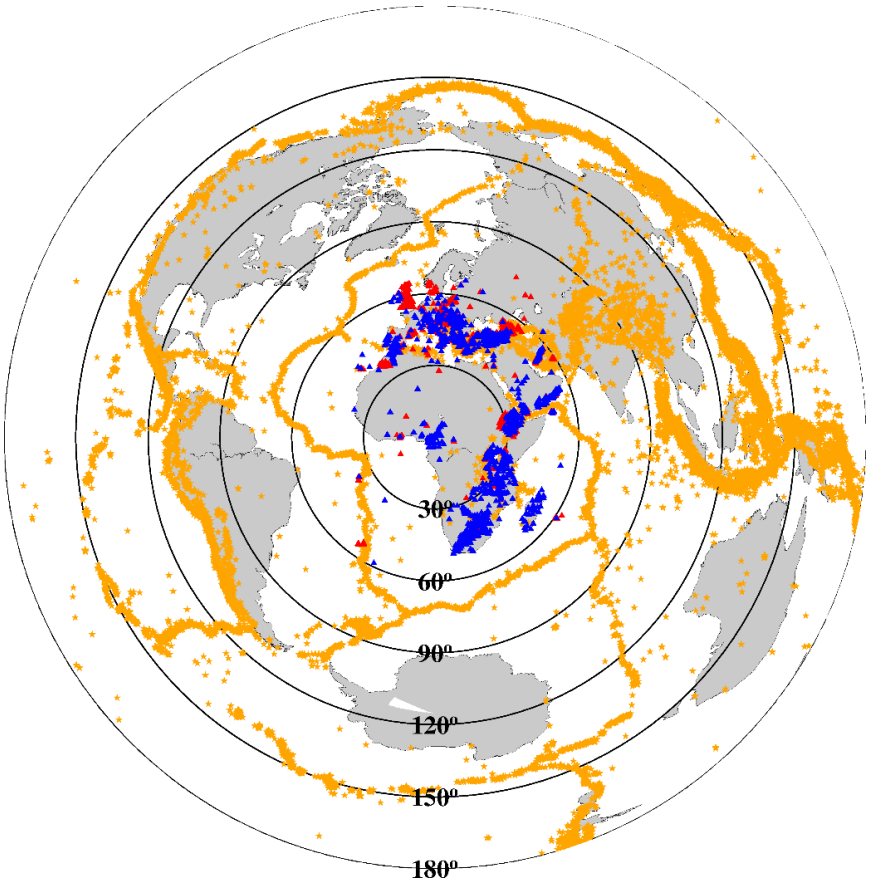

Figure 2. Distributions of broadband seismic stations (blue and red triangles) and earthquakes (yellow stars) used in this study. Red triangles highlight the seismic stations used only in ambient noise analysis. Note the global coverage and good azimuthal distribution of the events used.

To retrieve Rayleigh wave signals from earthquake records, we follow the traditional two-station method (e.g., Chen et. al., 2014; Kästle et al., 2016). As a first step, we select the appropriate event-station pairs that are assumed to travel along the same great-circle path. To achieve this, we set the thresholds in the angle differences between the great circles from the epicenter to the two stations (α) and between the great circles from the epicenter to the nearer station and from the nearer to the farther station (β) to 3° and 7°, respectively (e.g., Yao et al., 2010; Chen et al., 2014; Ojo et al., 2018). Next, we compute the signal-to-noise ratio (SNR) of each seismogram defined as the ratio of the peak amplitude in the signal window to

the root mean square of the noise in the noise window, both filtered with a specific central period (Bensen et al., 2007). Waveforms with SNRs less than 5 are discarded. The retained seismograms from the same event recorded by a selected station pairs are narrow-band-pass filtered after removing the instrument responses and cross-correlated to obtain the cross-correlation function (CCF, e.g., Yao et al., 2006). Finally, the positive lag-time sides of the CCFs between the same station pair obtained from all events are normalized and stacked together to obtain the final CCF for each station pair, which in turn, is used as input in the subsequent dispersion analysis.

3.3 Dispersion Analysis

Using the stacked NCFs and CCFs, we measure the fundamental mode phase and group velocities in the period range of 5–50 s by the automatic frequency-time analysis (AFTAN) with the appropriate phase shift for each dataset (Aki & Richards, 2002; Bensen et al., 2007; Shen & Ritzwoller, 2016). During the dispersion measurement, we use Rayleigh wave phase velocities from the global tomography model of Ma et al. (2014) as a reference to unwrap the 2-pi ambiguity of the phase velocities. We perform quality control to select the reliable dispersion measurements for the subsequent tomography based on the following criteria: (1) The inter-station distance must be greater than one wavelength to ensure sufficient separation of the surface wave packet from precursory arrivals and satisfy the far-field approximation (e.g., Luo et al., 2015). (2) The SNRs of the surface waves must be ≥ 8 to ensure the reliability of the signals. (3) The velocity dispersion data retained at every period must lay within the two standard deviations bound of the mean velocity calculated for all measurements at that period. The last step is to filter out the outliers of the dispersion measurements. Additionally, we visually inspect the dispersion curves to further discard bad measurements that could introduce artifacts in the tomographic inversion. We investigate the discrepancies between the resulting dispersion measurements from the two sources (ambient noise vs. earthquakes) for the same station pair at overlapping periods to understand the possible biases in our dataset. At overlapping periods, dispersion measurements with higher SNR are selected based on the assumption that they are obtained from a better-defined surface wave signal.

3.4 Inversion for Phase and Group Velocity Maps

To obtain the lateral variation of group and phase velocities in the study area, we perform tomographic inversions for the two-dimensional (2D) phase and group velocity maps at selected periods using the fast-marching surface-wave tomography (FMST) method (Sethian, 1996; Sethian & Popovici, 1999; Rawlinson & Sambridge, 2004, 2005; Rawlinson et al., 2006, 2008). FMST is an iterative nonlinear tomographic inversion method that solves the eikonal equation using the fast-marching method (FMM) based on the finite-difference approximations in a pre-defined grid for the forward modeling in 2D spherical surface

coordinates. A linearized subspace technique is used to solve the inverse problem (Kennett et al., 1988; Rawlinson & Sambridge, 2005). The key benefits of using this method are two-folded: (1) it does not need to repeat the travel-time computation for every ray path as in the traditional ray-tracing methods, and (2) it accounts for the non-linearity of the forward problem to provide stable and robust results even in strongly heterogeneous media (Rawlinson et al., 2010; Fang et al., 2016). We use the average velocity at each period as the starting velocity of the initial model. Since we do not have measurements associated with every station pair, the inverse problem is largely underdetermined, and regularization is needed to provide additional constraints on the model parameters and stabilize the inversion. Our choice of regularization parameters determined by the L-curve method (Aster et al., 2018) routinely favors models with smooth and small lateral velocity variations over models with sharp and large variations at each period.

3.5 Joint Inversion for Shear-wave Velocity Model

From the period-dependent Rayleigh wave phase and group velocity maps, we construct local dispersion curves extracted at 1° x 1° grid spacing and apply a joint inversion program based on the neighborhood algorithm (NA) of Sambridge (1999a,b) as in Ojo et al. (2019). An important advantage of choosing this method over the linearized method (e.g., Herrmann & Ammon, 2004) employed in most previous studies in Africa is its independence from the starting model and its ability to avoid local minimums. The method generates a random initial model based on the user-supplied ranges of model parameters, including layer thickness, velocity, Vp/Vs ratio, density, Qp, and Qs, determined from prior knowledge. The ranges of model parameters used in this study are chosen from literature (Kanamori & Anderson, 1977; Kennett et al., 1995; Brocher, 2005) and are listed in Table 1.

Table 1: Ranges of model parameters used in the NA inversion in this study

Layer ID	Thickness (km)	Top Vs (km/s)	Bottom Vs (km/s)	Vp/Vs	Qp	Qs
Crustal Layer-1	0–2	1.50 –4.00	1.50–4.00	2.00–3.00	100	25
Crustal Layer-2	0–3	1.50–4.00	1.50–4.00	1.65–2.00	675	300
Crustal Layer-3	1–15	2.60–4.50	2.60–4.50	1.65–1.80	1450	600
Crustal Layer-4	5–20	3.20–4.50	3.20–4.50	1.65–1.80	1450	600
Crustal Layer-5	5–20	3.20–4.50	3.20–4.50	1.65–1.80	1450	600
Mantle Layer-1	5 –30	4.00–5.00	4.00–5.00	1.70–1.90	1450	600

The efficient normal-mode formalism of Herrmann (2013) is used to compute the theoretical dispersions in the forward scheme and the objective function is defined as the least-square misfit between the observed and computed dispersions as follows:

$$M_{joint} = \sum_{j=1}^{2} w_j \cdot \sum_{i=1}^{N_j} \left[D_{ij}^{obs} - G_{ij}(m) \right]^2 \quad (1)$$

where j = 1, 2 refers to the group and phase velocities, respectively, weighted by w_j (with $w_1 = w_2 = 0.5$), $G_{ij}(m)$ and D_{ij}^{obs} are the synthetic and measured velocities, respectively, and N_j is the total number of measurements of a given velocity type. Based on our previous experience, we set the two tunable NA parameters that control how explorative and exploitative the inversion proceeds to be 100 and 60, respectively, and set a maximum of 1000 iterations producing an ensemble of 10100 models for each inversion point. The final 1D Vs model is the mean of all accepted ensemble of models from the surface to 60-km depth at each grid and the standard deviation is used to quantify the model uncertainty. At each grid point, we obtain an estimate of the crustal thickness by summing the thicknesses of the inverted crustal layers in the model ensemble and computing its mean and standard deviation.

4 Results and Interpretation

4.1 Emergence of Rayleigh Waves from Ambient Noise Cross Correlations

Figure 3 shows an example of the cross-correlations between the vertical-component ambient noise and earthquake records at station G.ATD and 46 other selected stations. Both the NCFs and CCFs yield a clear wave packet with a linear trend in arrival times, representing the fundamental mode Rayleigh waves with a moveout velocity of ~3.4 km/s (Shapiro & Campillo, 2004). Despite the different energy sources and methodology, the similarity in the symmetric NCFs and CCFs and dispersion curves indicates that both methods yield the same result and justifies the joint employment of the two datasets. Therefore, we combine them in the subsequent inversions to improve the resolution and achieve sensitivity to a broader depth range than previous studies (e.g., Kästle et al., 2018; Pourpoint et al., 2018).

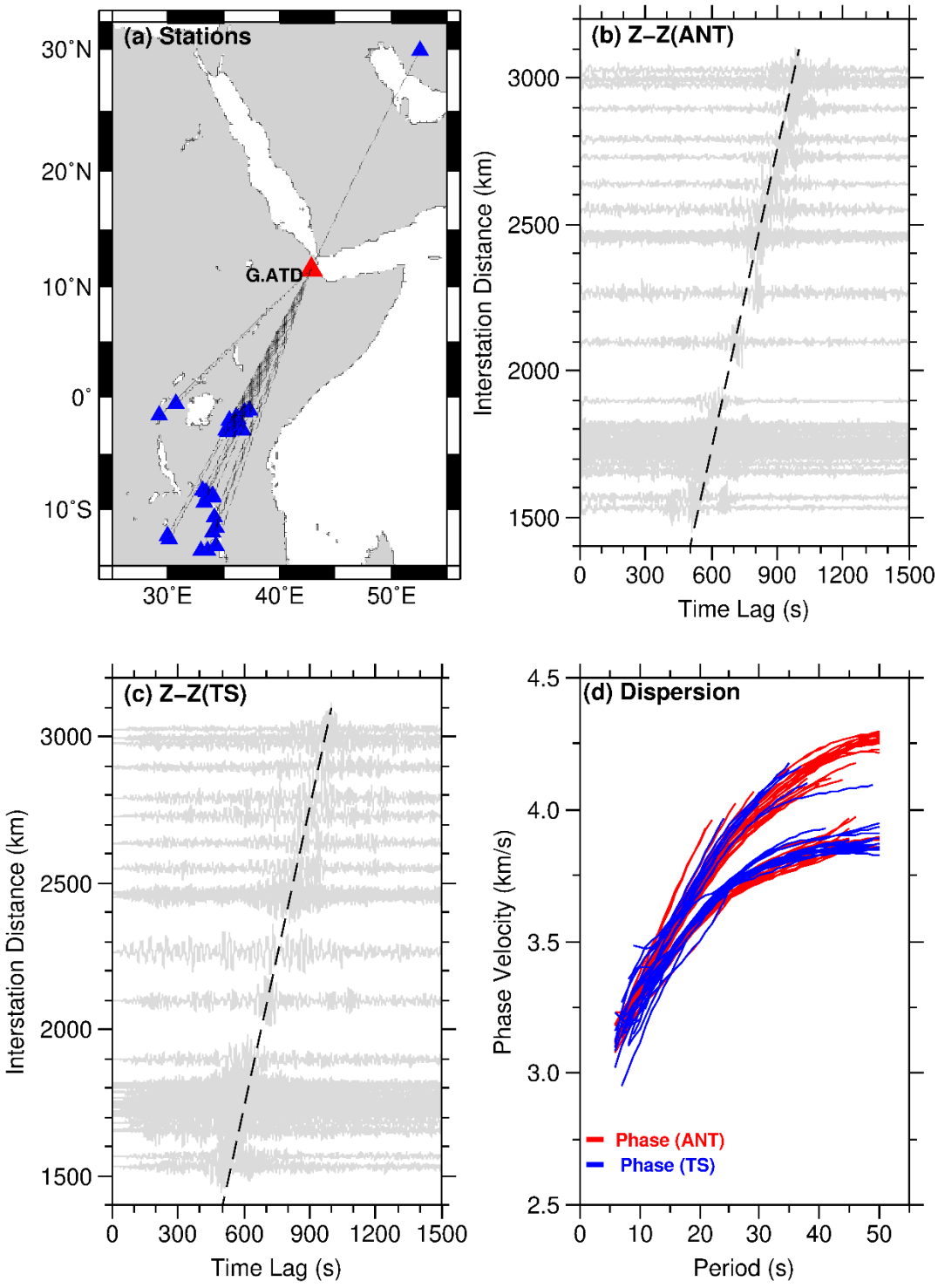

384

385 **Figure 3**. (a) Ray paths (thin black lines) between station G.ATD (red triangle) and 46 other seismic stations
386 (blue triangles) and representative stacked (b) NCFs and (c) CCFs filtered between 10 and 30 s (d) Phase
387 dispersion data retrieved from the NCFs and CCFs waveforms. The black dashed line indicates the arrival
388 times of the Rayleigh waves with a moveout of ~3.4 km/s.

4.2 Ray Path Coverage Improvement and Dispersion Discrepancy

Figure 4(a) shows the total number of paths available at each period in the final dataset used for the tomographic inversion after removing traces that do not meet the selection criteria mentioned in Section 3.3. The phase and group velocity measurements from the NCFs reveal two characteristic peaks corresponding to the primary (10–30 s) and secondary (5–10 s) microseisms. As expected, the maximum number of paths obtained is highest at short periods (< 15 s) for NCF measurements and at longer periods for the CCF analysis. To improve the resolution of the subsequent tomographic inversion, we combine the phase and group velocity measurements from NCFs and CCFs and achieve a significant improvement in the path coverage at overlapping periods (red in Figure 4a). The peak number of paths increases from ~25,000 (~15 s from NCFs) and ~30,000 (~25 s from CCFs) to ~50,000 at ~20 s when combined, enabling us to image the African continent at an unprecedented resolution. Figures 4(b-d) show the differences between the phase and group velocities obtained from NCFs and CCFs at overlapping periods of 15 s, 20 s, and 30 s. For dispersion measurements with high SNRs ≥ 10, the distribution of the phase-velocity differences follows a Gaussian distribution centered around ±0.01 km/s at 20 s and 30 s period and -0.02 km/s at 15 s; the mean differences are slightly larger for group velocity (-0.08 km/s at 15 s and 20 s, and -0.11 km/s at 30 s). The relatively small standard deviations suggest that the two types of measurements are consistent with each other and well within the typical range of uncertainties in dispersion measurement, i.e. ~1.5-1.7% of the average velocity (e.g., Yao et al., 2006, 2010; Ojo et al., 2018). The observed discrepancy can be attributed to different data sensitivity to heterogeneities and methodology (de Vos et al., 2013).

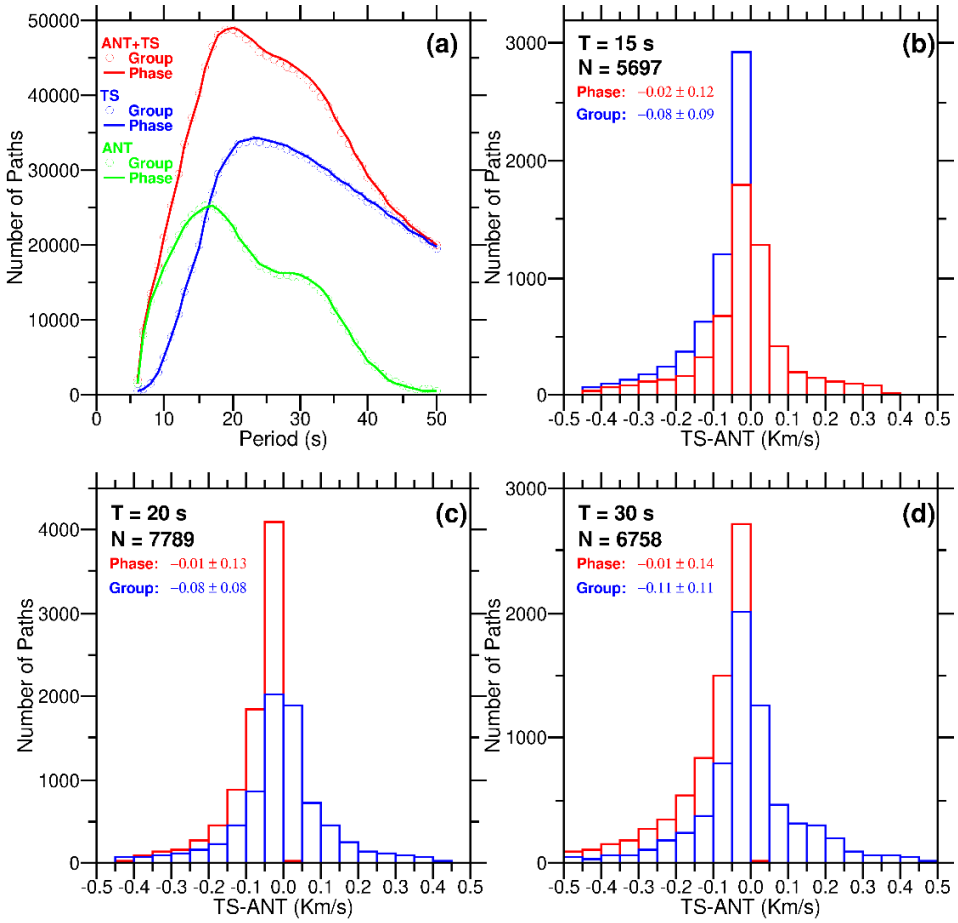

409

410 **Figure 4**. (a) Ray path count vs. period for the phase (solid lines) and group (circles) velocity measurements
411 obtained from records of ambient seismic noise (NCFs, green) and earthquakes (CCFs, blue). The total
412 number of paths of the combined NCF and CCF datasets is shown in red. (b), (c) and (d) Histograms of ray
413 path count for phase (red) and group (blue) velocity measurements at overlapping periods of 15 s, 20 s, and
414 30 s, respectively. The total number of paths (N) at each period is given for comparison. The mean
415 differences (km/s) between the NCF and CCF measurements and standard errors (km/s) are also noted for
416 phase and group velocities.

417

418 **4.3 Checkerboard Tests**

419 Despite its potential drawbacks, the checkerboard test is still valuable for investigating the capability of a
420 given station configuration to resolve the velocity structure across the study region (e.g., Leveque et al.,
421 1993; Simons et al., 2002; Rawlinson & Spakman, 2016). Therefore, we perform checkerboard tests at
422 different periods for varying cell sizes using the same inter-station ray paths for the observed data and the
423 optimal regularization parameters (e.g., Humphreys & Clayton, 1988; Inoue et al., 1990; Zhao, 2015). By
424 varying the cell size from 0.5° x 0.5° to 5° x 5° at an interval of 0.5° and reconstructing the checkerboard
425 based on the ray paths in the real dataset at different periods, we find the cell size of 3° x 3° to be the

minimum grid size that allows for satisfactory recovery of the checkerboard model across the entire continent. The checkerboard is not well resolved at smaller cell sizes especially at regions with sparse seismic stations (Figure 2). Figure 5(a) shows the 3° x 3° input model with a checkerboard pattern defined by peak velocity perturbations of ±0.4 km/s relative to the average velocity at each period and a bi-cubic B-spline interpolation between grid-nodes. Representative examples of the recovered checkerboard models with 3° x 3° cell size for group and phase velocities at periods of 8 s, 20 s, 30 s, and 50 s are provided in Figures 5(b-i). A comparison of the recovered checkerboard results to the input model gives us a basic impression of the different resolving powers by the data at different periods across the continent. At shorter periods (≤ 8 s; Figures 5b&c), the numbers of selected ray paths are insufficient to accurately resolve the 3° x 3° checkerboard pattern in the main part of northern Africa which is sparsely instrumented (see Figure 2). Signs of smearing with elongated anomalies trending in the NW-SE direction are obvious in the reconstructed models, indicating a deterioration in the resolution power. The ray path density becomes progressively improved with increasing periods, achieving the best ray path coverage at periods between 20 s and 30 s, and dropping again towards the longest period used in the study (see Figures 5d-i). As expected, we are unable to recover the checkerboard in areas outside of the data coverage. Because the lateral resolution is closely linked to the density and distribution of local stations as well as the number of ray paths, the checkerboard patterns are better resolved at all periods and cell sizes in eastern and southern Africa and southern parts of Europe. Meanwhile, the checkerboard test also demonstrates that the goal of this study to image the lithospheric structure in sparsely instrumented regions of the African continent is achievable with the available dataset.

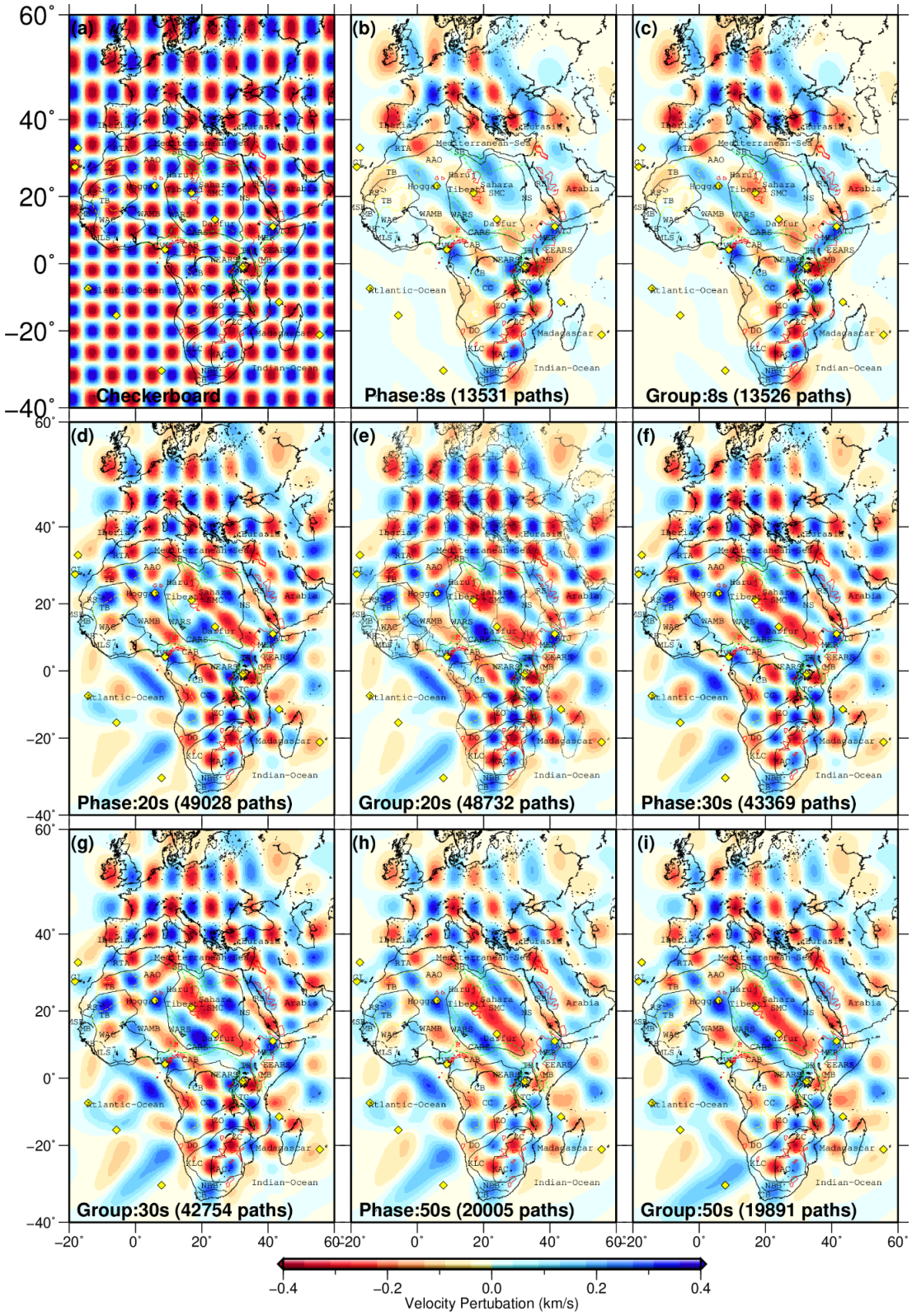

Figure 5. Checkerboard resolution test. (a) Checkerboard input model with a cell size of 3° x 3° and peak velocity perturbation of ±4%. (b-i) Recovered models of Rayleigh wave phase and group velocities at

periods of 8 s, 20 s, 30 s, and 50 s. Overlain on the plots are the geometry and locations of the main geological features across the study area as defined in Figure 1.

4.4 Phase and Group Velocity Maps

Figure 6 presents the Rayleigh wave phase and group velocity maps, and depth sensitivity kernels for periods of 10 s, 20 s, and 40 s. The depth sensitivity kernels indicate the depth ranges that contribute to the frequency-dependent velocity maps. Here, we simply provide a general description of the main features in the apparent velocity models, and interpretations of the inverted three-dimensional (3D) Vs models in terms of regional tectonics are presented in the subsequent sections.

At shorter periods (e.g., 10 s; Figures 6a&b), the peak sensitivities are in the range of ~0–10 km depth, and the phase and group velocity anomalies are generally consistent with surface geology with high velocities coinciding with cratonic units (e.g., KAC, ZC, TC, and UC) and low velocities in basins (e.g., CB, TB, and SB) underlain by thick sediments, as well as passive margins and hotspots (Figures 6a&b) (e.g., Yang et al., 2008; Domingues et al., 2016; Accardo et al., 2017; Pratt et al., 2017; Adams et al., 2018; Fadel et al., 2018; Adimah & Padhy, 2019; Chambers et al., 2019; Wang et al., 2019; Thybo et al., 2019). Outside of the African continent, the Arabian plate shows two distinct anomalies, fast velocity within the shield and low velocity farther into the interior platform (e.g., Tang et al., 2016; Yao et al., 2017; Kaviani et al., 2020). In southern Europe, the eastern Mediterranean Sea reveals a much lower velocity than the western part, and the Apennines are clearly outlined by low velocity (e.g., Yang et al., 2007; Kästle et al., 2018; Lu et al., 2018; Manu-Marfo et al., 2019).

At intermediate periods (e.g., 20 s; Figures 6c&d), the depth sensitivities peak in the ~10–25 km depth range and the resolution are more uniform due to increased ray paths (see Figure S1). The velocity maps show a general increase in velocity with depth, with fast anomalies in regions of relatively shallow oceanic crust (e.g., western Mediterranean and the Red Sea), rift zones (e.g., WARS), and cratonic units; while slow anomalies still coincide with regions of thick sediments, mobile belts and hotspots (e.g., Darfur).

At longer periods (e.g., 40 s; Figures 6e&f) corresponding to a greater depth, the velocity maps are more consistent with uppermost mantle structure and variations in the crustal thickness. Fast anomalies generally coincide with regions underlain by relatively thin crust while slow anomalies correspond to regions of relatively thick crust. Based on the normalized ray path densities, the resolution of the maps is poorest in the northwestern part of Africa and the surrounding oceans and best in eastern and southern Africa and southern Europe (see Figure S1). Generally, the pattern of anomalies on the group and phase velocity maps are similar at each period with slight differences that may be related to different depth sensitivities.

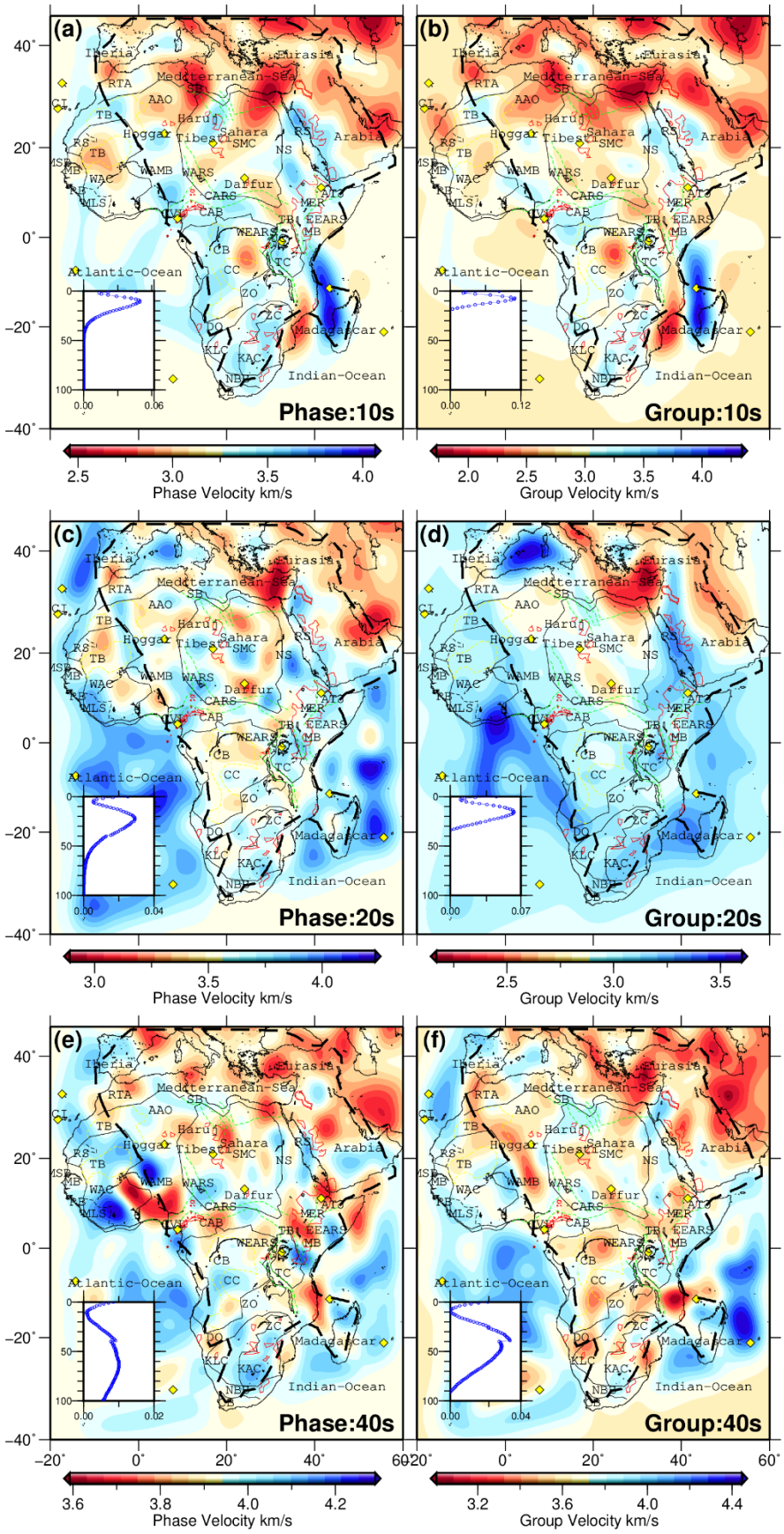
(a)
(b)
(c)
(d)
(e)
(f)
Phase:10s
Group:10s
Phase:20s
Group:20s
Phase:40s
Group:40s
Phase Velocity km/s
Group Velocity km/s
Eurasia
Iberia
Mediterranean-Sea
Arabia
Sahara
Tibesti
Hoggar
Harūj
Darfur
Atlantic-Ocean
Indian-Ocean
Madagascar

482

Figure 6. Maps of phase (a, c, e) and group (b, d, f) velocities at periods of 10 s, 20 s, and 40 s, with the inset plots showing the depth sensitivity kernels at the respective periods. Overlain on the plots are the geometry and locations of the main geological features across the study area as defined in Figure 1. The thick black dash line denotes the areas of the maps that are best resolved based on the ray path density.

4.5 1D Vs Models from Joint Inversions

In Figure 7, we present examples of the joint inversion result at four grid points located in different tectonic settings in western, eastern, northern, and southern Africa. Figure 7(a) shows the inverted Vs model along the CVL in western Africa characterized by low Vs at shallow depths underlain by a gradual increase of Vs with depth and the Moho at the depth of ~35 km. Figure 7(b) depicts a typical 1D Vs model within the cratonic units in southern Africa. The crust is relatively thick (~37 km) and characteristically fast Vs (~4 km/s) typical of cratonic crust can be seen from the upper crust down to the uppermost mantle. The Vs model in Figure 7(c) in eastern Africa near the Afar triple junction is characterized by a slow Vs (< 2.5 km/s) at shallow depths that persists down to the middle crust, typical of regions with active volcanism where magma exists within the crust (e.g., Chambers et al., 2019). Figure 7(d) shows an example of the inverted Vs model within the Rif-Tell-Atlas mountain belts in northern Africa, which reveals a relatively slow Vs at shallow depths underlain by a gradual increase of velocity with depth. The crustal thickness is ~39 km. Generally, we obtain characteristically smooth models that are geologically more plausible and consistent with the tectonic settings.

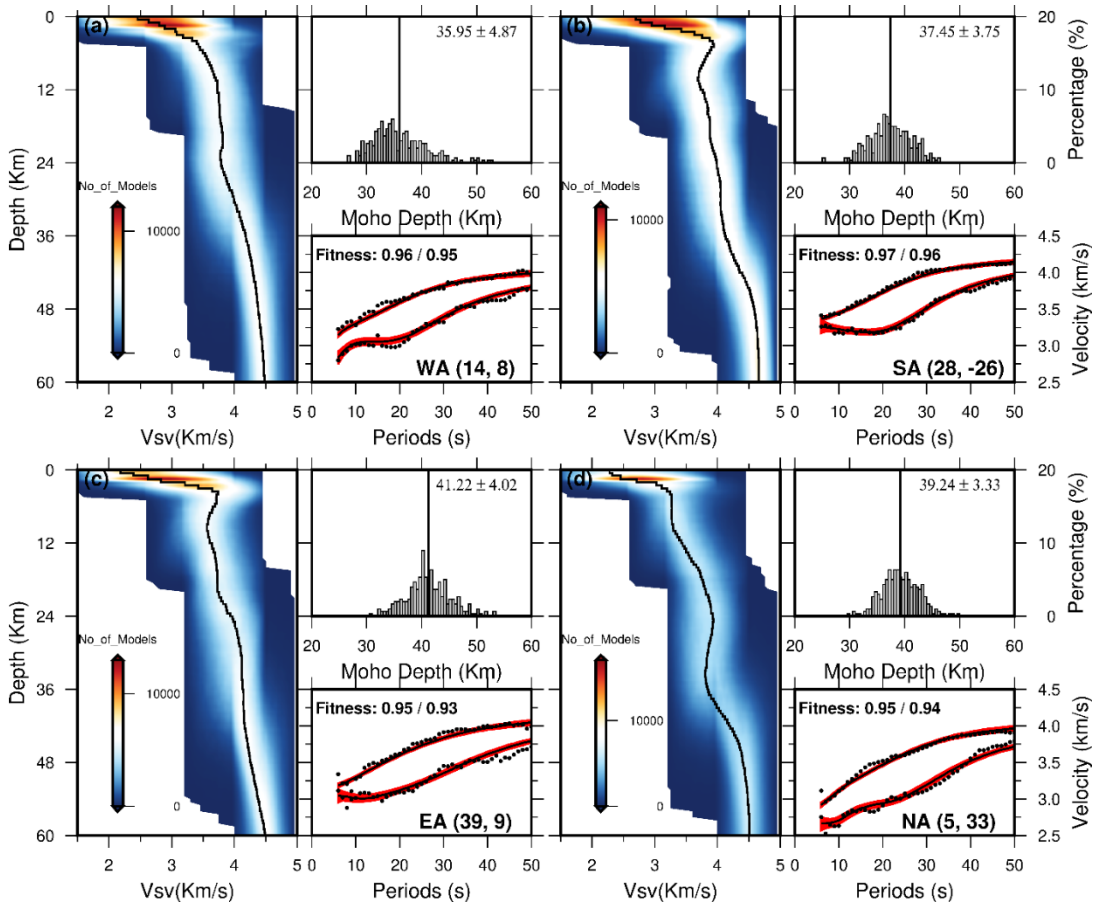

Figure 7. 1D Vs model jointly inverted from group and phase velocity data at four representative grid points located in (a) the CVL in western Africa, (b) the Kaapvaal craton in southern Africa, (c) the Afar Triple Junction in eastern Africa, and (d) the Rif-Tell-Atlas mountain belts in northern Africa. For each location, the left panel shows the mean 1D Vs model in a thick black line against the background of the ensembles of the 1D models sampled by the neighborhood algorithm. The upper-right panel displays the range of crustal thickness estimated from the 300 best-fitting models and the mean value (vertical black line) with associated uncertainty. The lower-right panel shows the observed dispersion data in black dots and predictions by the 300 best-fitting models and the mean Vs model in red and black lines, respectively. Also noted on the plot are the misfit values between the observed data and their theoretical predictions by the mean model.

4.6 Model Misfit

In Figure 8 we present the misfits between the group and phase velocity measurements and their theoretical counterparts predicted by the mean 1D Vs models at all grid points, following Ojo et al. (2019). A value of zero means a perfect fit between the theoretical and observed velocities while increasing values up to unity indicate a worsening fit. Figure 8 shows that at most grid points the misfit values are less than 0.1, and

much lower values are seen in regions with dense seismic stations. The group velocity seems to have a slightly larger misfit than the phase velocity, indicating a better fit by the final Vs model to the phase velocity measurements. A maximum misfit of 0.25 across the study area illustrates the overall goodness of data fit achieved in this study. It also demonstrates the robustness of the inversion scheme as well as the model parameterization which allows for satisfactory fits to both datasets for most of the study region (Ojo et al., 2019). The slightly larger misfit values beneath the sedimentary basins and surrounding oceanic regions indicate that it is necessary to investigate more closely the appropriate ranges of model parameters (Table 1) needed to fit the dataset at those locations.

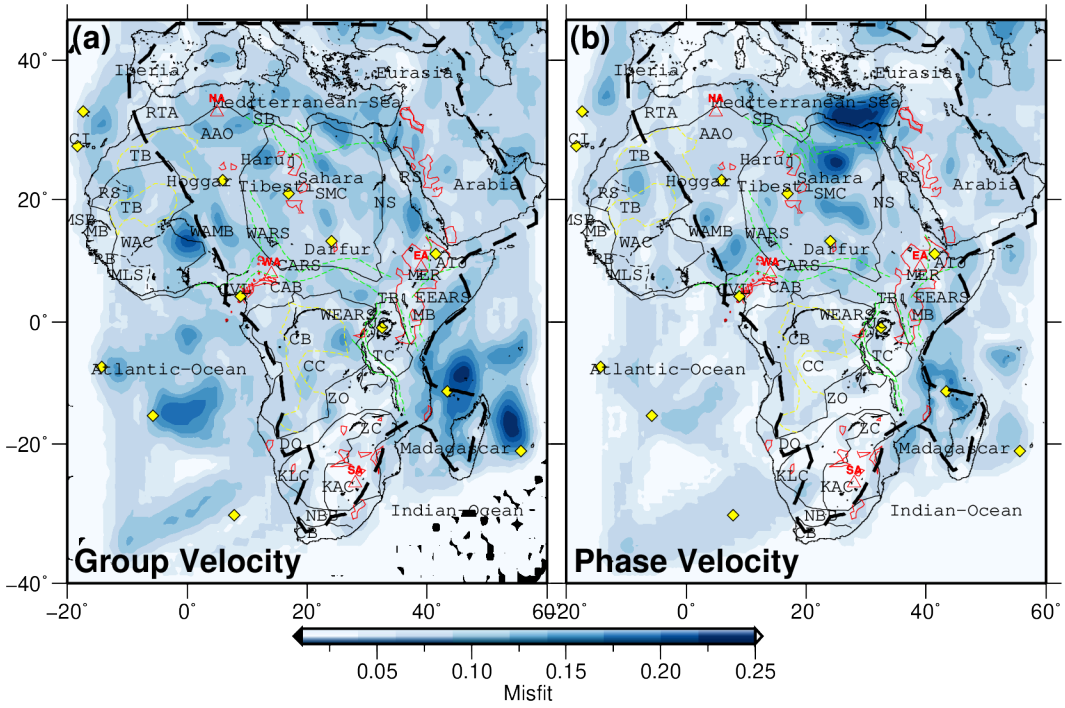

Figure 8. Maps of the misfits in (a) group and (b) phase velocities between the predictions by the mean 1D Vs model and the observed data. Red labels and triangles represent locations where joint inversion examples are presented in Figure 7. Overlain on the plots are the geometry and locations of the main geological features across the study area as defined in Figure 1. The thick black dash line denotes the areas of the maps that are best resolved based on the ray path density.

4.7 General Features of the 3D Vs Model

In Figure 9, we present the 3D Vs model at different depth ranges from the surface to the uppermost mantle. We divided the estimated crustal thickness (CT) into three equal thicknesses at each grid point and the average velocity at these depth ranges as proxies for the upper (0 - 1/3CT), middle (1/3CT – 2/3CT), and lower (2/3CT – CT) crust. Likewise, we define the uppermost mantle by averaging the velocity from the

estimated crustal thickness to the bottom of the model (CT – 60 km). We focus on structures within the defined region of best resolution denoted by the black thick line in Figure 9 to avoid interpreting possible artifacts.

In the upper crust (Figure 9a), relatively slow Vs (≤ 3 km/s) anomalies are observed at locations underlain by thick sediments (e.g., TB, CB, SB, Tyrrhenian Basin, Arabian Platform, etc.) and along zones of active deformation (e.g., MER, WARS, CARS, AAO, SMC, etc.) while relatively fast Vs (≥ 3.5 km/s) anomalies mainly coincide with cratons (e.g., KAC, ZC, UC, TC, etc.; Ebinger et al., 2017). The estimated sediment thickness in the uppermost crust ranges from 0 to 14.5 km and is consistent with the estimates of Laske & Masters (1997) across the study area (details in Text S1 and Figure S2). The structure in the mid crust (Figure 9b) shows a general increase in Vs in comparison to the upper crust but tends to be less heterogeneous (i.e. small velocity perturbation < 1 km/s). However, relatively fast Vs (≥ 4.0 km/s) can be observed at locations underlain by thin crust (e.g., Red Sea, etc.), along the edges of the Arabian plate, mobile belts, and orogens (e.g., WAMB, AAO, DO), Rift zones (e.g., CARS), and cratons (e.g., KAC). Relatively slow Vs (≤ 3.7 km/s) is pronounced within the Saharan metacraton and associated hotspots, Arabian Platform, eastern Tyrrhenian Basin, and around the Afar Tripple Junction (Figure 9b).

In the lower crust (Figure 9c), prominent fast Vs (≥4 km/s) anomalies are observed along the Red Sea, WAMB, western-to-central Mediterranean Sea. We also found thick layers (~5 – 15 km) of high-velocity (Vs ≥ 4.0 km/s) beneath cratonic units (e.g., WAC, CC, KAC), areas characterized by compressional and extensional tectonics (e.g., EARS, CARS), and locations of hotspot centers and diamond-rich kimberlites/lamproites, indicating the presence of mafic, high-density materials (details in Text S2 and Figure S2). Relatively slow Vs (≤ 4.0 km/s) is obvious beneath volcanic centers (e.g., Hoggar, Tibesti, and Darfur), western EARS, MER, southern Madagascar Island, northern CC, AAO, CB, and beneath some cratonic units (e.g., UC and ZC; Figure 9c). At this depth range, the spatial variation in Vs is strongly related to the crustal thickness across the study area, and the slow Vs may be in regions of thicker crust, while fast Vs may exist in regions of thinner crust. The estimated crustal thickness ranges from ~19 to 55 km and varies greatly both among and within the tectonic provinces of the African continent and the surrounding regions (details in Text S3 and Figure S3). In the uppermost mantle (Figure 9d), most of the study area is characterized by Vs ≥ 4.5 km/s. However, localized slow Vs (≤ 4.2 km/s) anomalies are found at several locations (e.g., WAMB, MER, SMC, RS, EARS, DO, SMC, TB, MB, TC, eastern Malawi Rift, and southwestern Madagascar; Figure 9d).

A detailed comparison of our 3D model with existing models from global/continental-scale studies (e.g., Laske et al., 2013; Schaeffer & Lebedev, 2013; Moulik & Ekstrom, 2014; Pasyanos et al., 2014; Celli et al., 2020) indicate greater agreement at mid-lower crustal and uppermost mantle depths within the estimated uncertainty of our model (details in Text S5; Figures S4 & S5). However, at upper crustal depth

and in sparsely instrumented regions of north-central and southwestern Africa, our model reveals more detailed features that correlate better with known tectonic features and we discussed this further in Section 5.1

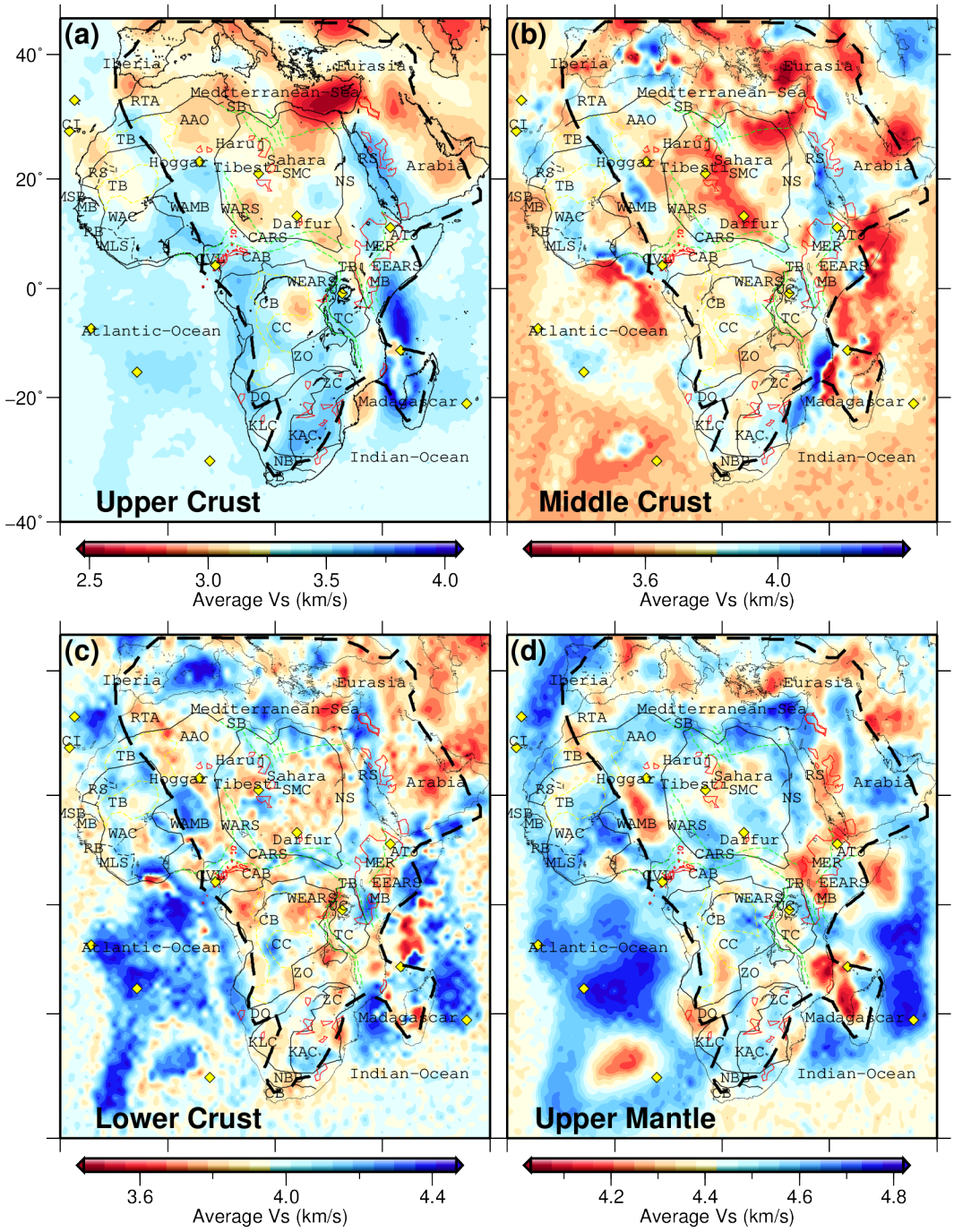

Figure 9. Shear wave velocity maps in four depth ranges across the study area. Vs anomalies are averaged over depth ranges within (a) the upper crust (b) the middle crust, (c) the lower crust, and (d) the upper mantle. See text for the definition of the depth ranges. Overlain on the maps are the geometry and locations

of the main geological features across the study area as defined in Figure 1. The thick black dash line denotes the areas of the maps that are best resolved based on the ray path density.

The average uncertainties at crustal and uppermost mantle depths range between 0 to 0.6 km/s but are generally less than 0.2 km/s in most of the study area as shown in Figures 10. The uncertainties reduce with increasing period included in the study reflecting the advantage of including dispersions from earthquake data. The map in the uppermost crust (Figure 10a) is characterized by slightly higher uncertainties (up to 0.3 km/s within the continent) while the map at uppermost mantle depths (Figure 10d) is associated with the lowest uncertainties (≤ 0.2 km/s).

4.8 Cross-sections Traversing Major Tectonic Blocks of Africa

For a more detailed description of the features in the 3D Vs model, we present four cross-sections traversing different tectonic regions in Africa and surrounding regions in Figure 11. The north-south profile AA' in Figure 11(a) traverses from the Cape belt, Namaqual-Natal and Kaapvaal craton in southern Africa through the Zambezi Orogen, the Congo craton, Central African belt, the Dafur hotspot, the Saharan metacratons into the Mediterranean Sea, and ends in the Alpinnes in southern Europe. A layer of slow Vs (≤ 3 km/s) delineates the location, geometry, and depth extents of sediments beneath different tectonic regions in the African uppermost crust. Low Vs is obvious down to ~15 km depth beneath the Congo craton, revealing the presence of thick sediment (e.g., Laske & Master, 1997; Figure S2). Similarly, low Vs extends progressively to greater depths from the Saharan desert into the northern margins, reaching to more than 15 km beneath the eastern Tyrrhenian Basin which is characterized by thick sediments (e.g., Lu et al., 2018). Underlying the Congo and Tyrrhenian Basin is a relatively shallow crust featuring fast Vs (≥ 4.2 km/s). Also, fast Vs (~4 km/s) is seen at both shallow and greater depths beneath the cratonic region (KC). Shear wave velocity is relatively slower beneath the Darfur region into the mid-lower crust, and a localized fast Vs layer is seen within the Saharan metacraton in this depth range. The lowermost crust reveals fast Vs (≥ 4 km/s) across the profile with varying thickness. Relatively fast Vs in the upper mantle is seen beneath the craton (KAC) and basins (CB and Tyrrhenian Basin) while the surrounding mobile belt reveals a relatively lower Vs. Shear wave velocities are slow (≤ 4.3 km/s) throughout the uppermost mantle beneath the Darfur hotspot and the Alpine region. The Moho depth varies across the profile with relatively shallow Moho (~30 km) beneath the Sahara metacraton and deep one (~45 km) beneath the Congo Basin.

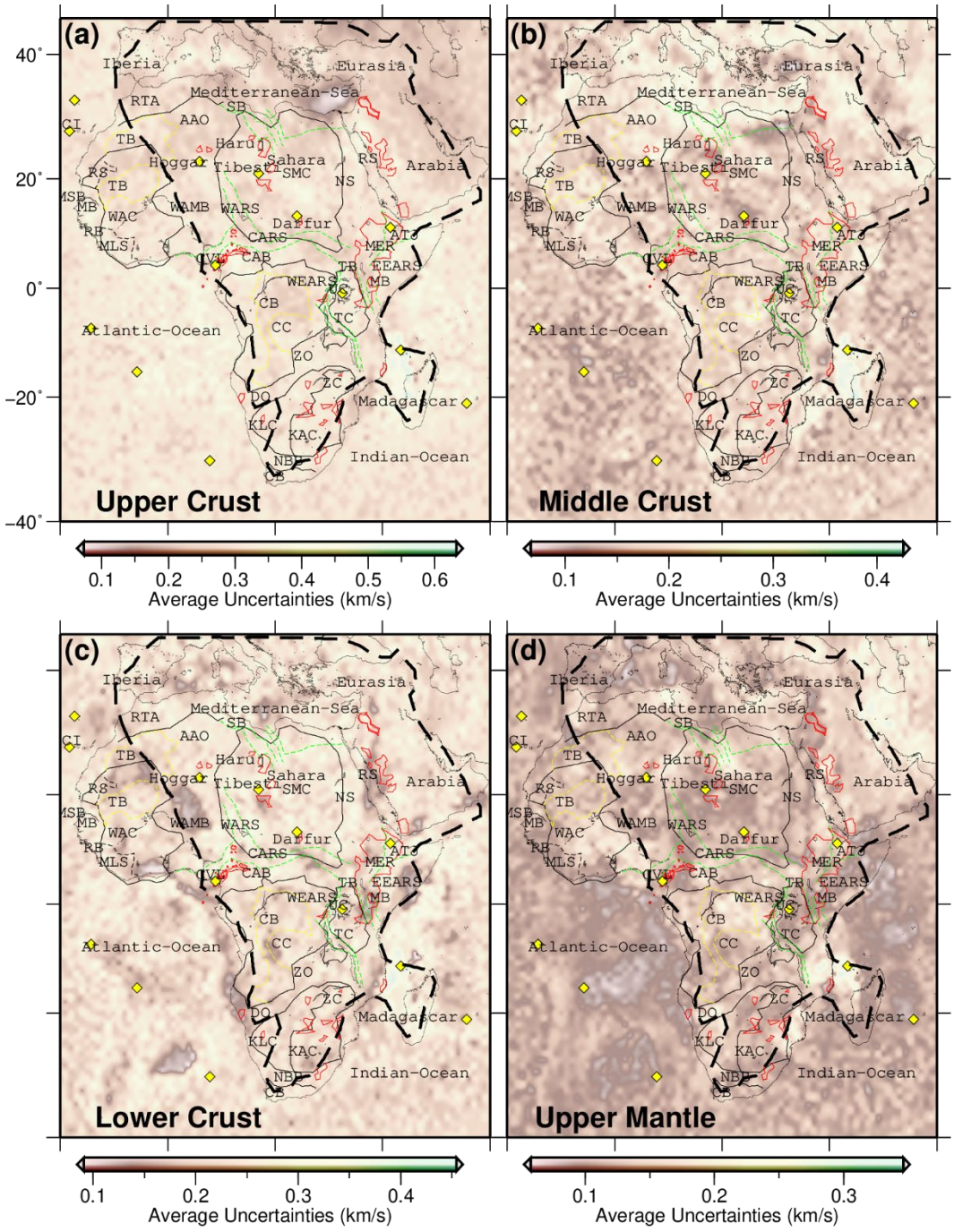

Figure 10. Average uncertainties of the 3D Vs model in four depth ranges across the study area. (a) the upper crust (b) the middle crust, (c) the lower crust, and (d) the upper mantle. See text for the definition of the depth ranges. Overlain on the maps are the geometry and locations of the main geological features across the study area as defined in Figure 1. The thick black dash line denotes the areas of the maps that are best resolved based on the ray path density.

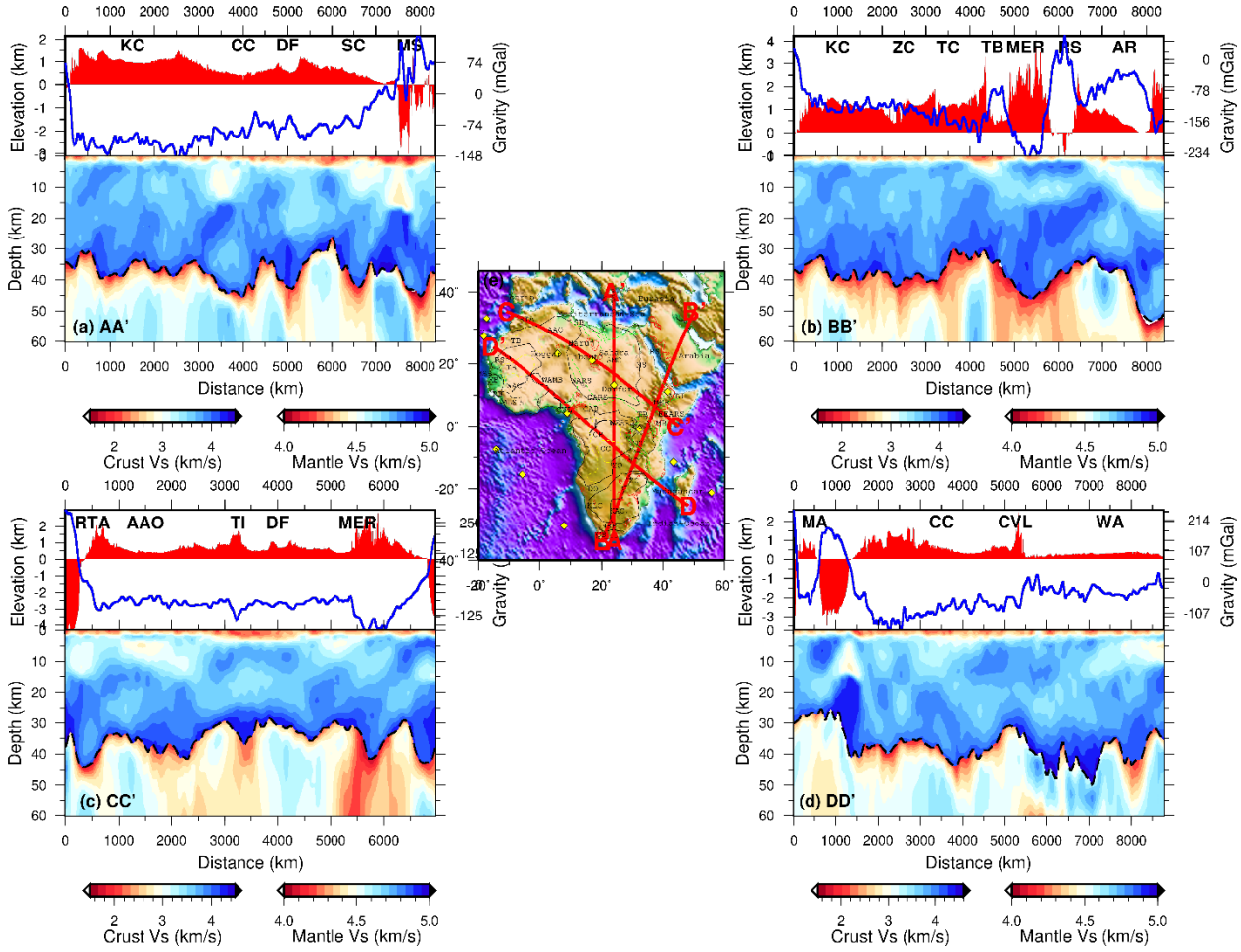

618

619 **Figure 11**. Cross-sections from the surface to 60-km depth along profiles (a) AA', (b) BB', (c) CC', and
620 (d) DD'. (e) Map of study region showing locations of the profiles in (a-d). Plotted on top of each cross-
621 section is the elevation from ETOPO1 (Amante & Eakins, 2009) in red and the Bouguer gravity anomaly
622 (EIGEN-6C4, Förste et al., 2014) profile in blue. The yellow diamonds in (e) mark locations of hotspots in
623 the study region and labels in black denote the main tectonic features as defined in Figure 1.
624
625 Profile BB' (Figure 11b) traverses from the Cape belt, Namaqual-Natal, and the cratonic units in
626 southeastern Africa (KAC, ZC, and TC) into the Main Ethiopian Rift, the Afar Triple Junction, the Red
627 Sea, and the Arabian plate. A very thin layer of slow Vs (≤ 3 km/s) is present across most of the profile but
628 extends to greater depths beneath thick sedimentary regions such as the Turkana Basin (~5 km) and the
629 Arabian platform (~ 20 km). Fast Vs (≥ 4km/s) characterizes the entire cratonic region down to the Moho
630 (~40 km), with a relatively shallower depth beneath the Tanzania craton (~35 km). A localized fast Vs layer
631 is obvious beneath the MER and the Red Sea, which may represent mafic bodies that cooled down within
632 the crust during magma eruption (e.g., Ebinger et al., 2017). Relatively slow Vs (≤ 4.4 km/s) is observed in
633 the uppermost mantle beneath the EARS, MER, and the Red Sea with evidence for magmatic underplating

and accompanying crustal thickening (~45 km/s). A similar observation is made at the edge of the profile beneath the Mesopotamian Foredeep Basin in eastern Arabia (e.g., Kaviani et al., 2020). Fast uppermost mantle Vs (≥ 4.6 km/s) is generally observed at greater depths within the mantle beneath the cratons (KC, TC, and UC) except for the Zimbabwe craton and the Arabian shield. The crust is relatively thin (~35 km) beneath the Arabian shield and thickens towards the Arabian platform and Mesopotamian Foredeep Basin (e.g., Kaviani et al., 2020).

Profile CC' in Figure 11(c) begins at the passive margin, enters the Rif-Tell Atlas mountain and the Anti-Atlas Orogen, crosses the West African Mobile Belt into the Saharan metacraton, Central African Belt, Ethiopian Plateau, and MER, then terminates at the eastern EARS. A thin layer of slow Vs (≤ 3 km/s) is obvious in the uppermost crust which persists to a greater depth (~ 5 km) beneath the Saharan metacraton and volcanic centers. A very thin layer of relatively fast Vs exists beneath the passive margin, Anti-Atlas Orogen, WAMB, and CAB but underlain by relatively slow Vs (≤ 3.2 km/s) down to a depth of ~15 km except for CAB where the slow Vs stops at ~8-km depth. We interpret the slow Vs beneath the passive margin as evidence for thick sediment, while the orogen and shear zone as an indication for a weakened crust. Localized fast Vs (≥ 4 km/s) zones are obvious beneath the Saharan Metacraton, probably indicating the presence of cratonic fragments or cooled mafic magma beneath the hotspots in the upper crust (e.g., Ojo et al., 2019). The lower crust along the profile is generally characterized by fast Vs (≥ 4km/s). The Moho is relatively deep beneath the Rif-Tell Atlas mountain (~45 km), consistent with isostatic compensation. The Moho is at ~43-km depth beneath the MER and plateau, and shallower beneath the Saharan metacratons, Darfur region, and eastern EARS (~30–35 km). Pronounced slow upper mantle Vs (≤ 4.4 km/s) is seen beneath the MER and eastern EARS, indicating the presence of high temperature and partial melting or upwelling of magma probably from the sub-lithospheric mantle (e.g., Civiero et al., 2016; Chambers et al., 2019). The overlying deep Moho may reflect ongoing magmatic underplating, the continued addition of mafic material to the base of the lower crust. Similarly, relatively slow Vs (≤ 4.5 km/s) can be seen in the uppermost mantle beneath the Saharan metacraton region. Here, the slow Vs may be related to magma upwelling beneath the Tibesti volcanic center and other nearby hotspots. The uppermost mantle Vs is relatively fast (≥ 4.6 km/s) beneath the Rif-Tell Atlas mountain, Anti-Atlas Orogen, and the Central African Belt.

Figure 11(d) shows the profile DD' which begins from the Madagascar Island, traverses the Indian Ocean, Mozambique Basin, Zambezi Orogen, Congo craton, CVL, Benue Trough, and terminates near the West African craton. A thin layer of slow Vs (≤ 3 km/s) is seen in the uppermost crust across the profile. The region of southern Madagascar is underlain by Vs < 4 km/s at crustal depths. Fast Vs (≥ 4 km/s) characterizes the Indian Ocean crust that thins into the Mozambique Basin at the edge of the continent. Slow Vs extending to the depth of ~15 km at this location indicates the presence of thick sediment beneath

the continent-ocean passive margin. The Zambezi Orogen and Congo Basin are characterized by relatively slow Vs (≤ 3.5 km/s) in the mid-upper crust, while thick layers of fast Vs are obvious beneath the Congo Basin in the lower crust. Localized fast Vs is obvious beneath the northern part of Congo craton and Benue Trough in the mid-upper crust (~10–20 km depth). The Taoudeni Basin within the West African craton is characterized by relatively slow Vs (≤ 3.2 km/s), indicating sediment as thick as ~10 km trapped beneath a thin layer of fast Vs. The profile is underlain by a lower crust of fast Vs (≥ 4 km/s). The crust is relatively thin (≤ 30 km) beneath southern Madagascar, Indian Ocean, and southern CVL (e.g., Ojo et al., 2019), while the Moho depth at other locations along the profile is ~35–45 km. The uppermost mantle Vs is relatively slow (≤ 4.5 km/s) beneath the Indian Ocean, Zambezi Orogen, Congo Basin, CVL, and Taoudeni Basin, whereas faster Vs (≥ 4.6 km/s) is mainly seen beneath parts of the Congo and the West African craton. A relatively slow uppermost mantle Vs beneath Mt. Cameroon, the only active volcano along the CVL, may indicate the possibility of small-scale mantle upwelling as proposed by several authors (e.g., Adams et al., 2018). This is supported by the presence of localized fast Vs anomaly in the mid-lower crust beneath the region, which may be resulted from cooled mafic body intruded into the crust during magma transport and eruption (e.g., Ojo et al., 2018, 2019).

5 Discussion

5.1 Seismic Evidence for Cratonic Remnants within the Saharan Metacraton

One of the main achievements of this study is the ability to reliably image the lithospheric structures in aseismic regions with sparse broadband seismic stations in Africa (Figure 2). An important example of such a location is north-central Africa which plays host to the poorly imaged Saharan Metacraton. The term "Saharan Metacraton" was put forward by Abdelsalam et al. (2002) to indicate that the cratonic unit in this area has been partially destroyed and highly remobilized during the Neoproterozoic time and has since lost its characteristically cold, thick, and dense subcontinental lithospheric mantle (SCLM) during collisional processes. Three cratonic remnants (Murzuq, Al-Kufrah, and Chad) overlain by sedimentary basins and separated by topographic swells, including Hoggar, Tibesti Massif, and Darfur Dome has been suspected to exist in this region (e.g., Fezaa et al., 2010; Abdelsalam et al., 2011; Liégeois et al., 2013; Sobh et al., 2020). To find seismic evidence for the existence of these suspected cratonic remnants, we present four cross-sections of our 3D Vs model across the proposed boundary of the SMC in Figure 12 and several horizontal slices together with the crustal thickness map across the region in Figure S6.

Figure 12(a) shows a profile traversing the Cameroon Volcanic Line, the Chad Basin (overlying the Chad cratonic remnant), and terminating at the northern end of the Al-Kufrah Basin (overlying the Al-Kufrah cratonic remnant). In the upper crust, we find slow Vs (≤ 3 km/s) which persists to a depth of ~8 km beneath the Chad Basin, indicating the existence of thick sediment. The sediment is thinner (< 5 km) at

the southern edge of the Al-Kufrah basin and becomes thicker towards the northern edge (Figure 12a). Underlying the sediment are localized fast velocity anomalies (≥ 4 km/s) typical of cratonic remnants at a shallow depth (< 10 km) beneath the Al-Kufrah basin and deeper (> 10 km) beneath the Chad Basin. We interpret the observed localized fast Vs bodies as likely cratonic remnants from the metacratonization process (Abdelsalam et al., 2002). The uppermost mantle beneath the Chad Basin is characterized by relatively fast Vs (≥ 4.5 km/s), whereas the mantle Vs beneath the Al-Kufrah basin is relatively slow (≤ 4.5 km/s).

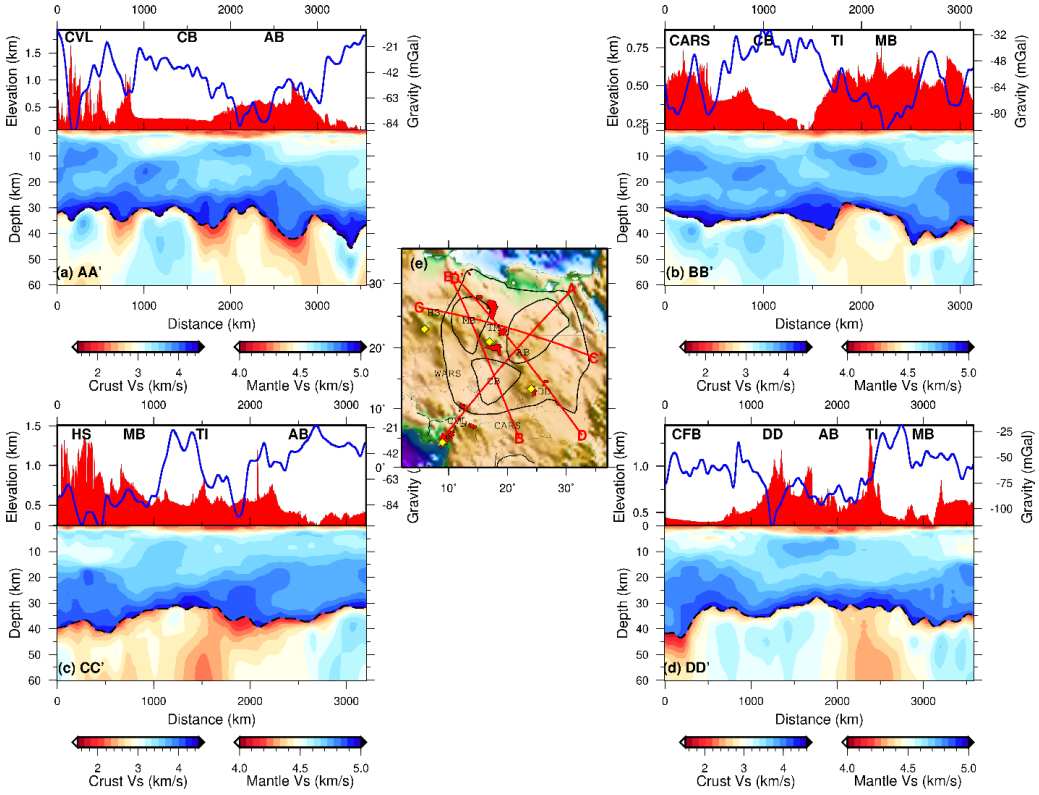

Figure 12. Cross-sections from the surface to 60-km depth along profiles (a) AA', (b) BB', (c) CC', and (d) DD'. (e) Map of study region showing locations of the profiles in (a-d) across the Saharan Metcraton, with black lines indicating the boundaries of the suspected cratonic remnants (Liégeois et al., 2013). Plotted on top of each cross-section is the elevation from ETOPO1 (Amante & Eakins, 2009) in red and the Bouguer gravity anomaly (EIGEN-6C4, Förste et al., 2014) profile in blue. The yellow diamonds in (e) mark locations of hotspots in the study region.

Profile BB' traverse the Central Africa Rift System (CARS) into the Chad and Murzuq basins and terminating outside the SCM (Figure 12b). Beneath this profile, the Murzuq basin is characterized by relatively thin sediment (~2 km) underlain by a localized fast Vs body in the uppermost crust and a slow Vs in the uppermost mantle.

In profile CC' (Figure 12c), slow Vs (≤ 3 km/s) persists down to ~15-km depth around the Hoggar hotspot on top of a thick layer of fast Vs and a slow upper mantle. Beneath the Murzuq and Al-Kufrah basins in Profile CC' (Figure 12c), the cratonic remnant is not obvious in the mid-lower crust, suggesting that the fast Vs body is limited to the southern part of the inferred boundaries. However, the underlying mantle Vs is relatively slow as observed in profile BB'. Relatively slow mantle Vs and less dense Bouguer gravity anomaly are found beneath the Tibesti hotspot underlain by obvious mantle upwelling (Figures 12c&d). Such an anomalously slow upper mantle Vs continues to a greater depth and has been observed in the global/continental-scale tomographic models (e.g., Fishwick, 2010; Schaeffer & Lebedev, 2013; Emry et al., 2019). This also agrees with the observation of Sobh et al. (2020) who found high temperatures related to mantle upwelling beneath the Tibesti hotspot. We also note that outside of the cratonic remnant and swells, the other parts of SMC are characterized by relatively fast upper mantle Vs.

In profile DD' (Figure 12d), localized fast Vs observed in profile AA' is also present at the southern edge of the Al-Kufrah basin underlain by a Vs of ~4.5 km/s in the uppermost mantle. The mantle upwelling beneath the Tibesti hotspot is also obvious in profile DD'. Comparing the three previously identified cratonic remnants, we find small negative Bouguer gravity anomaly (low density) and relatively fast uppermost mantle Vs beneath the Chad basin (Figures 12a&b), whereas larger negative Bouguer gravity anomaly (high density) and relatively slow uppermost mantle Vs are found beneath both the Murzuq and Al-Kufrah basins (Figures 12b&d). Likewise, the cratonic remnant beneath the Chad basin reveals more homogeneous velocity distribution within the inferred boundaries, while the structures differ in the southern (faster Vs) and northern (slower Vs) parts of the Murzuq and Al-Kufrah cratonic remnants (Figure S6). Sobh et al. (2020) observed that the Al-Kufrah cratonic remnant is characterized by higher density and lower temperature and is different from the Murzuq and Chad cratonic remnants. Based on our 3D model, a larger portion of the Al-Kufrah cratonic remnant in the north is characterized by slower Vs than the other two cratonic remnants, which is consistent with the observation of Sobh et al. (2020). We note that the three previously reported cratonic remnants are not located entirely within the boundaries inferred by Liégeois et al. (2013), as seen in the horizontal slices of our 3D Vs model in Figure 12(e). Rather, the geometry and locations of the fast Vs bodies that are best revealed by our model at mid-lower crustal depth (~25–40 km) indicate a northward offset (Figure 12e). Against the argument of Liégeois et al. (2005), we observe unique mantle upwellings beneath each of the intra-cratonic Cenozoic volcanic swells (i.e. Hoggar, Tibesti, and Darfur Dome), suggesting that they may be fed by unconnected plumes (Burke, 1996; Wilson & Guiraud, 1992; Sebai et al., 2006; Montagner et al., 2007).

Seismic estimates of the crustal thickness around the SMC are limited because of the sparsity of seismic station, and estimates from gravity modeling are subjected to high uncertainty due to trade-offs with mantle density anomalies (Herceg et al., 2016; Sobh et al., 2020). However, our new model reveals

that the crustal thicknesses in areas around and within the SMC range from ~28 to 52 km (Figure 12f). Thick crust (~40–45 km) is observed in the northern part of SMC encompassing the northern part of the Al-Kufrah basin whereas the western part of SMC is characterized by a crustal thickness of ~36 km. However, thin-crust (≤ 30km) underlies the south-central part of SMC including the southern part of the Murzuq and Al-Kufrah basins and the entire Chad basin. A circular region that encompasses the southern portion of the inferred cratonic remnant boundaries and most of the southwestern part of the Chad basin delineates the area of thin crust (≤ 32 km). This area is surrounded by a much thicker crust (~34–40 km) within the SMC (Figure 12f).

Previous studies suggested that the destruction of the interior of the former emplaced craton in the Sahara region can be attributed to several collisional events along its edges, including collisions with the Arabian-Nubian Shield to the east, the Tuareg Shield and West African Craton to the west, the Congo Craton to the south and an unnamed continent to the north. It has been hypothesized that the collisions probably led to the shortening (i.e. crustal thickening) and subsequent delamination of the sub-continental lithospheric mantle along zones of weakness within the craton, followed by high-temperature metamorphism as well as magma generation (Abdelsalam et al., 2002, 2011; Liégeois et al., 2005, 2013; Sobh et al., 2020). Results based on our 3D lithospheric model indicate that a combination of collisional events along the craton edges in addition to widespread Cenozoic volcanism may have contributed significantly to the metacratonization of the originally emplaced craton (Figures 12 and S6). This is evidenced by the emplacement of several localized fast Vs bodies within the SMC and the existence of thick crust around the SCM but the thin crust in the central-southern part of the remobilized craton (Figures 12e & f).

5.2 Secular Variation in Crustal Genesis

Knowledge about the nature of the Precambrian crust is important for developing geodynamic models of crustal genesis and evolution (Kachingwe et al., 2015). Since most parts of the African continent and Arabia are underlain by Precambrian crust (Milesi et al., 2010), several studies have tried to establish the relationship between crustal parameters and basement geologic age to advance our understanding of the formation and evolution of the continental crust. However, different results have been obtained by different research groups, leading to a continuing debate in the literature with some arguing for an obvious relationship (e.g., Durrheim & Mooney, 1991, 1994; Thompson et al., 2010; Abbott et al., 2013), while others claiming no discernible relation (e.g., Rudnick & Fountain, 1995; Al-Damegh et al., 2005; Kennett et al., 2011; Tugume et al., 2012, 2013; Stankiewicz & De Wit, 2013; Kachingwe et al., 2015).

To contribute to this important discussion, we compare the estimated crustal properties from this study to the age of the underlying basement rocks (e.g., Tugume et al., 2013). In Table 2, we list our estimated

thicknesses and average velocities in the upper, middle, lower, and whole crust as well as the thickness of High-Velocity Layer (HVL) in the lower crust with respect to the ages of Archean and Proterozoic terranes compiled by Tugume et al. (2013). We find variations in the crustal properties among and within individual geological provinces that are related to the local geological settings. For example, in the Archean terrains, thick fast velocity layers (> 10 km) underlain the North Limpopo Belt and Witwatersrand Terrane, whereas other Archean provinces are underlain by relatively thin layers (< 5 km) characterized by much faster velocity.

Table 2. Comparison between the estimated crustal properties from this study and the ages of underlying rocks in southern and eastern Africa and the Arabian Shield from Tugume et al. (2013).

Longitude (°)	Latitude (°)	Location	Geologic Age	Crustal Thickness (km)	HVL Thickness (km)	Avg. Upper Crust (km/s)	Avg. Middle Crust (km/s)	Avg. Lower Crust (km/s)	Avg. Crustal Velocity (km/s)
33.3	-5.1	Dodoman Terrane	Archean	30.15	2.16	3.51	3.74	3.93	3.72
33.6	-2.4	Nyanzian Terrane	Archean	31.65	2.95	3.44	3.84	3.95	3.74
24.1	-21.4	Magondi Belt	Archean	34.01	2.17	3.42	3.72	3.91	3.68
28.2	-21	Central Limpopo Belt	Archean	34.55	3.47	3.52	3.83	3.95	3.76
14.7	2.8	Congo Craton	Archean	35	1.83	3.56	3.77	3.8	3.71
29.8	-18.3	East Towke Terrane	Archean	35.76	1.77	3.52	3.69	3.9	3.7
32.1	-20.9	South Limpopo Belt	Archean	37.91	2.49	3.52	3.77	3.98	3.75
26.4	-27.8	Witwaterstand Terrane	Archean	38.27	12.44	3.57	3.87	4.15	3.86
33.8	-18.8	North Limpopo Belt	Archean	39.07	11.74	3.38	3.74	4.08	3.74
24.7	-25.5	Kimberley Terrane	Archean	39.65	4.72	3.61	3.81	3.96	3.79
30.3	-25.9	Swaziland Terrane	Archean	41.51	1.45	3.57	3.92	3.96	3.81
30.9	-22.6	Pietersbug Terrane	Archean	44.37	1.51	3.57	3.91	3.83	3.77
Average Archean				36.83 ± 3.92	4.06 ± 3.70	3.52 ± 0.07	3.80 ± 0.07	3.95 ± 0.09	3.75 ± 0.05
12.7	4.7	Oubanguide Belt	Proterozoic	29.7	2.05	3.47	3.85	3.84	3.72
25.6	-18	Okwa Terrane	Proterozoic	33.5	2.2	3.41	3.73	3.91	3.68
31.4	1.5	Rwenzori Belt	Proterozoic	33.77	0.81	3.43	3.66	3.67	3.59
21.8	-29.6	Namaqua Natal Belt	Proterozoic	33.9	2.52	3.57	3.76	3.89	3.74
30	-2.4	Kibaran Belt	Proterozoic	34.15	1.42	3.48	3.76	3.82	3.69
30.3	-5.2	Ubendian Belt	Proterozoic	34.64	2.01	3.49	3.77	3.88	3.71
43.3	24.3	Afif Terrane	Proterozoic	34.99	2.15	3.27	3.76	3.77	3.6
35.2	-7.6	Usagaran Belt	Proterozoic	35.34	4.92	3.48	3.71	4	3.73
41.2	20.9	Asir Terrane	Proterozoic	37.15	9.25	3.57	3.9	4	3.82
38.2	-1	Mozambique Belt	Proterozoic	37.23	11.64	3.43	3.77	4.22	3.8
43.9	19.8	Nabitah Terrane	Proterozoic	37.66	2.96	3.47	4.02	3.95	3.81
27.3	-19	West Tokwe Terrane	Proterozoic	37.87	7.94	3.5	3.73	4.06	3.76
45.2	22.3	Af Ryan Terrane	Proterozoic	38.23	5.02	3.29	3.78	3.99	3.69
22.6	-25.6	Kheis Province	Proterozoic	39.39	2.91	3.53	3.74	3.94	3.73
Average Proterozoic				35.54 ± 2.46	4.13 ± 3.15	3.46 ± 0.09	3.78 ± 0.09	3.92 ± 0.13	3.72 ± 0.07

In the Archean terranes, the crust is thick (> 40 km) beneath the Swaziland and Pietersburg terranes but thin (~30 km) beneath the Dodoman and Nyanzian terranes. Similarly, in the Proterozoic terranes, the Oubanguides Belt and Okwa terranes are underlain by relatively thin crust (< 34 km), while thick crust (> 38 km) exists beneath the Af Ryan Terrane and Kheis Province. Variations of up to ~0.3 km/s in Vs are seen among and within the Archean and Proterozoic terranes (Table 2). The average crustal thicknesses are 36.83 ± 3.92 km and 35.54 ± 2.46 km in the Achaean and Proterozoic terranes, respectively, indicating similarity within the estimated uncertainties. Likewise, the mean thickness of HVL in the lower crust, which

could indicate compositional differences, is also similar (i.e. 4.06 ± 3.70 km beneath the Achaean terrain and 4.13 ± 3.15 km beneath the Proterozoic terrain). The average velocity differences between the Archean and Proterozoic terranes in the upper, mid, lower, and the entire crust are less than 0.1 km/s and also fall within the estimated uncertainties. Therefore, we do not find an obvious relationship between the estimated average crustal properties and the ages of the underlying basement rocks within the two terranes, in agreement with some previous observations (e.g., Tugume et al., 2012, 2013; Kachingwe et al., 2015). Previous authors with similar findings have indicated that this may be due to changes in the process that formed the continental crust overtime or the crust in different provinces may have been significantly modified by tectonic processes (e.g., lower crustal flow or foundering of eclogites into the mantle) such that no discernible relations have been preserved (e.g., Rey et al., 2001; Zandt et al., 2004).

6 Conclusions

In this study, we use ambient seismic noise and earthquake data recorded by broadband seismic stations in Africa, Europe, and Arabia for the past three decades to develop a new continental-scale 3D Vs model for the African continent and the surrounding regions. The 3D Vs model shows slow Vs anomalies that coincide with locations of thick sediments, zones of active deformation, and places where magma bodies are present within the crust; while fast Vs regions correlate with cratonic units and thin oceanic crust (e.g., Pasyanos & Nyblade, 2007). In the mid-lower crust, fast Vs reveals the geometry and locations of mafic bodies that intruded into the crust and characterizes areas underlain by a relatively thin crust, while slow Vs is found in regions underlain by thick crust and hotspots. Slow uppermost mantle Vs anomalies is seen beneath mobile belts, hotspots, magma-assisted rift areas, and metacratons; while cratonic roots, mountain belts, and basins are associated with fast Vs. The estimated crustal thickness in the study area range from ~20 to 55 km. The thickest crust is found beneath the cratons, whereas the thinnest crust is found in oceanic and volcanic regions. We find thick layers of fast Vs in the lower crust around intra-cratonic basins, areas of active rifting, continental margins, oceans as well as hotspot centers, and locations of diamond-rich kimberlites/lamproites indicating the presence of mafic high-density materials. However, their formation and/or removal mechanisms are controlled mainly by local tectonics in different parts of the study region.

Our tomography inversion achieved an unprecedented resolution in sparsely instrumented regions such as north-central Africa where the poorly imaged Saharan Metacraton (SMC) is located. As a result, we provide the first seismic evidence that confirms the existence of three suspected cratonic remnants (Murzuq, Al-Kufrah, and Chad remnants) buried beneath thick sediments within the SMC and constrains their locations and geometry. We also imaged distinct mantle upwelling beneath Hoggar, Tibesti Massif, and Darfur Dome hotspots that they may be fed by unconnected plumes. The anomalies in our 3D Vs model shows a better correlation with known tectonic features in the upper crust than the existing continental-

scale models (e.g., Laske et al., 2013). At uppermost mantle depths, our model is consistent with the existing continental-scale and global models within the estimated uncertainties (e.g., Schaeffer & Lebedev, 2013; Moulik & Ekstrom, 2014; Celli et al., 2020). Our new improved model can improve earthquake detection and location in Africa that can lead to much better performance in the monitoring practice of the Comprehensive Nuclear-Test-Ban Treaty. Our results are also useful for regional seismic hazard analysis and geodynamic modeling studies. We make the model publicly available and hope to continue updating it as time and funding allow.

Acknowledgments

The entire seismic dataset used in this study is publicly available and retrieved from the IRIS Data Management Center (IRIS-DMC; https://ds.iris.edu/ds/nodes/dmc/, last accessed July 2018). We thank all the network managers and participants of several experiments in Africa that contributed data to IRIS-DMC. This research was supported by National Natural Science Foundation of China (41590854). This work was also supported by the Academic Development Projects 7101302050, 7101302500 and 7101500121 of Peking University. O. A. O acknowledges the support of the Boya Postdoctoral Fellowship of Peking University and thank Desbarats Alexandre (Natural Resources Canada) for mentorship. We would like to thank Yingjie Yang (Macquarie University, Sydney, Australia) for helpful discussion of the manuscript. Most of the maps presented in the paper were created using the Generic Mapping Tools (Wessel et al., 2013). Sac2000 (Goldstein et al., 2003) and the Standing Order for Data (SOD) program of Owens et al. (2004) were used for basic seismic data retrieving and processing.

References

Abbott, D. H., Mooney, W. D., & VanTongeren, J. A. (2013). The character of the Moho and lower crust within Archean cratons and the tectonic implications. *Tectonophysics*, 609, 690-705.

Abdelsalam, M., Gao, S., & Liégeois, J. (2011). Upper mantle structure of the Saharan Metacraton. *Journal of African Earth Sciences*, *60*(5), 328-336. doi: 10.1016/j.jafrearsci.2011.03.009

Abdelsalam, M., Liégeois, J., & Stern, R. (2002). The Saharan Metacraton. *Journal of African Earth Sciences*, *34*(3-4), 119-136. doi: 10.1016/s0899-5362(02)00013-1

Accardo, N., Gaherty, J., Shillington, D., Ebinger, C., Nyblade, A., & Mbogoni, G. et al. (2017). Surface wave imaging of the weakly extended Malawi Rift from ambient-noise and teleseismic Rayleigh waves from onshore and lake-bottom seismometers. *Geophysical Journal International*, *209*(3), 1892-1905. doi: 10.1093/gji/ggx133

Accardo, N., Gaherty, J., Shillington, D., Hopper, E., Nyblade, A., & Ebinger, C. et al. (2020). Thermochemical Modification of the Upper Mantle Beneath the Northern Malawi Rift Constrained From Shear Velocity Imaging. *Geochemistry, Geophysics, Geosystems*, *21*(6). doi: 10.1029/2019gc008843

Adams, A., Miller, J., & Accardo, N. (2018). Relationships Between Lithospheric Structures and Rifting in the East African Rift System: A Rayleigh Wave Tomography Study. *Geochemistry, Geophysics, Geosystems*, *19*(10), 3793-3810. doi: 10.1029/2018gc007750

Adams, A., Nyblade, A., & Weeraratne, D. (2012). Upper mantle shear wave velocity structure beneath the East African plateau: evidence for a deep, plateauwide low velocity anomaly. *Geophysical Journal International*, *189*(1), 123-142. doi: 10.1111/j.1365-246x.2012.05373.x

Adimah, N., & Padhy, S. (2019). Ambient noise Rayleigh wave tomography across the Madagascar island. *Geophysical Journal International*, *220*(3), 1657-1676. doi: 10.1093/gji/ggz542

Agius, M., & Lebedev, S. (2013). Tibetan and Indian lithospheres in the upper mantle beneath Tibet: Evidence from broadband surface-wave dispersion. *Geochemistry, Geophysics, Geosystems*, *14*(10), 4260-4281. doi: 10.1002/ggge.20274

Aki, K., & Richards, P. G. (2002). *Quantitative seismology*.

Albaric, J., Deverchere, J., Perrot, J., Jakovlev, A., & Deschamps, A. (2014). Deep crustal earthquakes in North Tanzania, East Africa: Interplay between tectonic and magmatic processes in an incipient rift. *Geochemistry, Geophysics, Geosystems*, *15*(2), 374-394.

Al-Damegh, K., Sandvol, E., & Barazangi, M. (2005). Crustal structure of the Arabian plate: new constraints from the analysis of teleseismic receiver functions. *Earth and Planetary Science Letters*, 231(3-4), 177-196.

Amante, C., & Eakins, B. W. (2009). ETOPO1 arc-minute global relief model: procedures, data sources and analysis.

Aster, R. C., Borchers, B., & Thurber, C. H. (2018). Parameter estimation and inverse problems. Elsevier.

Ayarza, P., Alvarez-Lobato, F., Teixell, A., Arboleya, M. L., Teson, E., Julivert, M., & Charroud, M. (2005). Crustal structure under the central High Atlas Mountains (Morocco) from geological and gravity data. *Tectonophysics*, *400*(1-4), 67-84.

Bagley, B., & Nyblade, A. A. (2013). Seismic anisotropy in eastern Africa, mantle flow, and the African superplume. *Geophysical Research Letters*, *40*(8), 1500-1505.

Bailey, D. K. (1992). Episodic alkaline igneous activity across Africa: Implications for the causes of continental break-up. Geological Society,London, Special Publications, 68(1), 91–98. https://doi.org/10.1144/GSL.SP.1992.068.01.06

Bastow, I. D., Nyblade, A. A., Stuart, G. W., Rooney, T. O., & Benoit, M. H. (2008). Upper mantle seismic structure beneath the Ethiopian hot spot: Rifting at the edge of the African low-velocity anomaly. *Geochemistry, Geophysics, Geosystems*, *9*(12).

Begg, G. C., Griffin, W. L., Natapov, L. M., O'Reilly, S. Y., Grand, S. P., O'Neill, C. J., ... & Bowden, P. (2009). The lithospheric architecture of Africa: Seismic tomography, mantle petrology, and tectonic evolution. *Geosphere*, *5*(1), 23-50.

Benoit, M. H., Nyblade, A. A., Owens, T. J., & Stuart, G. (2006). Mantle transition zone structure and upper mantle S velocity variations beneath Ethiopia: Evidence for a broad, deep-seated thermal anomaly. *Geochemistry, Geophysics, Geosystems*, *7*(11).

Bensen, G. D., Ritzwoller, M. H., Barmin, M. P., Levshin, A. L., Lin, F., Moschetti, M. P., ... & Yang, Y. (2007). Processing seismic ambient noise data to obtain reliable broad-band surface wave dispersion measurements. *Geophysical Journal International*, *169*(3), 1239-1260.

Boschi, L., & Ekström, G. (2002). New images of the Earth's upper mantle from measurements of surface wave phase velocity anomalies. *Journal of Geophysical Research: Solid Earth*, *107*(B4), ESE-1.

Bosworth, W., Huchon, P., & McClay, K. (2005). The red sea and gulf of aden basins. *Journal of African Earth Sciences*, *43*(1-3), 334-378.

Brocher, T. M. (2005). Empirical relations between elastic wavespeeds and density in the Earth's crust. *Bulletin of the seismological Society of America*, *95*(6), 2081-2092.

Brown, C., & Girdler, R. W. (1980). Interpretation of African gravity and its implication for the breakup of the continents. *Journal of Geophysical Research: Solid Earth*, *85*(B11), 6443-6455.

Burke, K. (1996), The African plate, S. Afr. J. Geol., 99, 339–410.

Butcher, L. A., K. H. Mahan, and J. M. Allaz (2017), Late Cretaceous to Paleocene crustal hydration in the Colorado Plateau, USA, from xenolith petrology and monazite geochronology, Lithosphere, 9, doi:10.1130/L583.1.

Čadek, O., & Martinec, Z. (1991). Spherical harmonic expansion of the Earth's crustal thickness up to degree and order 30. *Studia Geophysica et Geodaetica*, *35*(3), 151-165.

Cahen, L., Snelling, N., Delhal, J., & Vail, J. (1984). The geochronology and evolution of Africa. Oxford: Clarendon Press.

Campillo, M., & Paul, A. (2003). Long-range correlations in the diffuse seismic coda. *Science*, *299*(5606), 547-549.

Celli, N. L., Lebedev, S., Schaeffer, A. J., & Gaina, C. (2020). African cratonic lithosphere carved by mantle plumes. *Nature communications*, *11*(1), 1-10.

Chambers, E. L., Harmon, N., Keir, D., & Rychert, C. A. (2019). Using ambient noise to image the northern East African Rift. *Geochemistry, Geophysics, Geosystems*, *20*(4), 2091-2109.

Chen, H., Zhu, L., Wang, Q., Zhang, P., & Yang, Y. (2014). S-wave velocity structure of the North China from inversion of Rayleigh wave phase velocity. *Journal of Asian Earth Sciences*, *88*, 178-191. doi: 10.1016/j.jseaes.2014.03.006

Chesler, R. (2012), The Geochemistry and Geochronology of Tanzanian Kimberlites, School of Earth Sci., The Univ. of Melbourne, Melbourne.

Chevrot, S., & Zhao, L. (2007). Multiscale finite-frequency Rayleigh wave tomography of the Kaapvaal craton, *Geophysical Journal International*, 169, 201-215, doi:10.1111/j.1365-246X.2006.03289.x.

Chorowicz, J. (2005), The East African Rift System, *J. Afr. Earth Sci*., 43, 379–410.

Christensen, N. I., & Mooney, W. D. (1995). Seismic velocity structure and composition of the continental crust: A global view. *Journal of Geophysical Research: Solid Earth*, *100*(B6), 9761-9788.

Civiero, C., Goes, S., Hammond, J. O., Fishwick, S., Ahmed, A., Ayele, A., ... & Leroy, S. (2016). Small-scale thermal upwellings under the northern East African Rift from S travel time tomography. *Journal of Geophysical Research: Solid Earth*, *121*(10), 7395-7408.

Coffin, M. F., & Rabinowitz, P. D. (1987). Reconstruction of Madagascar and Africa: evidence from the Davie fracture zone and western Somali basin. *Journal of Geophysical Research: Solid Earth*, *92*(B9), 9385-9406.

Collins, A. (2006). Madagascar and the amalgamation of Central Gondwana. *Gondwana Research*, *9*(1-2), 3-16. doi: 10.1016/j.gr.2005.10.001

Condie, K. C., Archean andesites, in Andesites, edited by R. S. Thorpe, p. 575 – 590, John Wiley, NY, 1982.

Cornell, D. H., Thomas, R. J., Gibson, R., Moen, H. F. G., Reid, D. L., Moore, J. M., & Gibson, R. L. (2006). The Namaqua-Natal Province. Geological Society of South Africa.

Craig, T. J., Jackson, J. A., Priestley, K., & McKenzie, D. (2011). Earthquake distribution patterns in Africa: their relationship to variations in lithospheric and geological structure, and their rheological implications. *Geophysical Journal International*, *185*(1), 403-434.

962 Crosby, A. G., Fishwick, S., & White, N. (2010). Structure and evolution of the intracratonic Congo
963 Basin. *Geochemistry, Geophysics, Geosystems*, *11*(6).
964 de Vos, D., Paulssen, H., & Fichtner, A. (2013). Finite-frequency sensitivity kernels for two-station surface wave
965 measurements. *Geophysical Journal International*, *194*(2), 1042-1049.
966 De Wit, M. J., de Ronde, C. E., Tredoux, M., Roering, C., Hart, R. J., Armstrong, R. A., ... & Hart, R. A. (1992).
967 Formation of an Archaean continent. *Nature*, *357*(6379), 553-562.
968 de Wit, M. J. (2003). Madagascar: Heads it's a continent, tails it's an island, Annu. Rev. Earth Planet. Sci., 31(1),
969 213–248.
970 Deen, T. J., Griffin, W. L., Begg, G., O'Reilly, S. Y., Natapov, L. M., & Hronsky, J. (2006). Thermal and
971 compositional structure of the subcontinental lithospheric mantle: Derivation from shear wave seismic
972 tomography. *Geochemistry, Geophysics, Geosystems*, *7*(7).
973 Domingues, A., Silveira, G., Ferreira, A. M., Chang, S. J., Custódio, S., & Fonseca, J. F. (2016). Ambient noise
974 tomography of the East African Rift in Mozambique. *Geophysical Journal International*, *204*(3), 1565-
975 1578.
976 Dorbath, C., Dorbath, L., Fairhead, J. D., & Stuart, G. W. (1986). A teleseismic delay time study across the
977 Central African Shear Zone in the Adamawa region of Cameroon, West Africa. *Geophysical Journal*
978 *International*, *86*(3), 751-766.
979 Ducea, M., & Saleeby, J. (1998). A case for delamination of the deep batholithic crust beneath the Sierra Nevada,
980 California. *International Geology Review*, *40*(1), 78-93.
981 Durrheim, R. J., & Nyblade, A. A. (2019). AfricaArray studies of the lithosphere in sub-Saharan Africa. *Acta*
982 *Geologica Sinica-English Edition*, *93*, 22-24.
983 Durrheim, R. (2008). Africa Array. Quest, 4(2), 14-15.
984 Durrheim, R. J., & Mooney, W. D. (1991). Archean and Proterozoic crustal evolution: Evidence from crustal
985 seismology. *Geology*, 19(6), 606-609.
986 Durrheim, R. J., & Mooney, W. D. (1994). Evolution of the Precambrian lithosphere: seismological and
987 geochemical constraints. *Journal of Geophysical Research: Solid Earth*, 99(B8), 15359-15374.
988 Ebinger, C. (2005). Continental break-up: the East African perspective. *Astronomy & Geophysics*, *46*(2), 2-16.
989 Ebinger, C. J. (1989). Tectonic development of the western branch of the East African rift system. *Geological*
990 *Society of America Bulletin*, *101*(7), 885-903.
991 Ebinger, C. J., & Sleep, N. H. (1998). Cenozoic magmatism throughout east Africa resulting from impact of a
992 single plume. *Nature*, *395*(6704), 788-791.
993 Ebinger, C. J., Deino, A. L., Drake, R. E., & Tesha, A. L. (1989). Chronology of volcanism and rift basin
994 propagation: Rungwe volcanic province, East Africa. *Journal of Geophysical Research: Solid*
995 *Earth*, *94*(B11), 15785-15803.
996 Ebinger, C. J., Oliva, S. J., Pham, T. Q., Peterson, K., Chindandali, P., Illsley-Kemp, F., ... & Gaherty, J. (2019).
997 Kinematics of active deformation in the Malawi Rift and Rungwe Volcanic Province,
998 Africa. *Geochemistry, Geophysics, Geosystems*, *20*(8), 3928-3951.
999 Eglington, B. M., & Armstrong, R. A. (2004). The Kaapvaal Craton and adjacent orogens, southern Africa: a
1000 geochronological database and overview of the geological development of the craton. *South African*
1001 *Journal of Geology*, *107*(1-2), 13-32.
1002 Emry, E. L., Shen, Y., Nyblade, A. A., Flinders, A., & Bao, X. (2019). Upper mantle earth structure in Africa
1003 from full-wave ambient noise tomography. *Geochemistry, Geophysics, Geosystems*, *20*(1), 120-147.

Endrun, B., Lebedev, S., Meier, T., Tirel, C., & Friederich, W. (2011). Complex layered deformation within the Aegean crust and mantle revealed by seismic anisotropy. *Nature Geoscience*, *4*(3), 203-207.

Erdman, M. E., Lee, C. T. A., Levander, A., & Jiang, H. (2016). Role of arc magmatism and lower crustal foundering in controlling elevation history of the Nevadaplano and Colorado Plateau: A case study of pyroxenitic lower crust from central Arizona, USA. *Earth and Planetary Science Letters*, *439*, 48-57.

Faccenna, C., Becker, T. W., Lucente, F. P., Jolivet, L., & Rossetti, F. (2001). History of subduction and back arc extension in the Central Mediterranean. *Geophysical Journal International*, *145*(3), 809-820.

Faccenna, C., Piromallo, C., Crespo-Blanc, A., Jolivet, L., & Rossetti, F. (2004). Lateral slab deformation and the origin of the western Mediterranean arcs. *Tectonics*, *23*(1).

Fadel, I., van der Meijde, M., & Paulssen, H. (2018). Crustal structure and dynamics of Botswana. *Journal of Geophysical Research: Solid Earth*, *123*(12), 10-659.

Fagereng, Å. (2013). Fault segmentation, deep rift earthquakes and crustal rheology: Insights from the 2009 Karonga sequence and seismicity in the Rukwa–Malawi rift zone. *Tectonophysics*, *601*, 216-225.

Fairhead, J. D., & Okereke, C. S. (1988). Depths to major density contrats beneath the West African rift system in Nigeria and Cameroon based on the spectral analysis of gravity data. *Journal of African Earth Sciences (and the Middle East)*, *7*(5-6), 769-777.

Fang, H., Zhang, H., Yao, H., Allam, A., Zigone, D., Ben-Zion, Y., ... & van der Hilst, R. D. (2016). A new algorithm for three-dimensional joint inversion of body wave and surface wave data and its application to the Southern California plate boundary region. *Journal of Geophysical Research: Solid Earth*, *121*(5), 3557-3569.

Faure, S., Godey, S., Fallara, F., & Trépanier, S. (2011). Seismic architecture of the Archean North American mantle and its relationship to diamondiferous kimberlite fields. *Economic Geology*, *106*(2), 223-240.

Fezaa, N., Liégeois, J. P., Abdallah, N., Cherfouh, E. H., De Waele, B., Bruguier, O., & Ouabadi, A. (2010). Late Ediacaran geological evolution (575–555 Ma) of the Djanet Terrane, Eastern Hoggar, Algeria, evidence for a Murzukian intracontinental episode. *Precambrian Research*, *180*(3-4), 299-327.

Fischer, K. M. (2002), Waning buoyancy in the crustal roots of old mountains, Nature, 417, 933–936.

Fishwick, S. (2010). Surface wave tomography: Imaging of the lithosphere–asthenosphere boundary beneath central and southern Africa?. *Lithos*, *120*(1-2), 63-73. doi: 10.1016/j.lithos.2010.05.011

Fishwick, S., & Bastow, I. D. (2011). Towards a better understanding of African topography: a review of passive-source seismic studies of the African crust and upper mantle. *Geological Society, London, Special Publications*, *357*(1), 343-371.

Fitton, J., & Dunlop, H. (1985). The Cameroon line, West Africa, and its bearing on the origin of oceanic and continental alkali basalt. *Earth and Planetary Science Letters*, *72*(1), 23-38. doi: 10.1016/0012-821x(85)90114-1

Forte, A. M., Moucha, R., Simmons, N. A., Grand, S. P., Rowley, D. B., & Mitrovica, J. (2010). New Insights into the Basin and Swell Dynamics of Africa Driven by Whole-Mantle Convection. *AGUFM*, *2010*, T23F-06.

Foster, K., Dueker, K., Schmandt, B., & Yuan, H. (2014). A sharp cratonic lithosphere–asthenosphere boundary beneath the American Midwest and its relation to mantle flow. *Earth and Planetary Science Letters*, *402*, 82-89.

Frizon de Lamotte, D., Saint Bezar, B., Bracène, R., & Mercier, E. (2000). The two main steps of the Atlas building and geodynamics of the western Mediterranean. *Tectonics*, *19*(4), 740-761.

Funck, T., Louden, K. E., & Reid, I. D. (2001). Crustal structure of the Grenville Province in southeastern Labrador from refraction seismic data: evidence for a high-velocity lower crustal wedge. *Canadian Journal of Earth Sciences*, *38*(10), 1463-1478.

Furman, T., Bryce, J. G., Karson, J., & Iotti, A. (2004). East African Rift System (EARS) plume structure: insights from Quaternary mafic lavas of Turkana, Kenya. *Journal of Petrology*, *45*(5), 1069-1088.

George, R., Rogers, N., & Kelley, S. (1998). Earliest magmatism in Ethiopia: evidence for two mantle plumes in one flood basalt province. *Geology*, *26*(10), 923-926.

Globig, J., Fernàndez, M., Torne, M., Vergés, J., Robert, A., & Faccenna, C. (2016). New insights into the crust and lithospheric mantle structure of Africa from elevation, geoid, and thermal analysis. *Journal of Geophysical Research: Solid Earth*, *121*(7), 5389-5424.

Goldstein, P., Dodge, D., Firpo, M., Minner, L., Lee, W. H. K., Kanamori, H., ... & Kisslinger, C. (2003). SAC2000: Signal processing and analysis tools for seismologists and engineers. The IASPEI international handbook of earthquake and engineering seismology, 81, 1613-1620.

Grand, S. P. (2002). Mantle shear–wave tomography and the fate of subducted slabs. *Philosophical Transactions of the Royal Society of London. Series A: Mathematical, Physical and Engineering Sciences*, *360*(1800), 2475-2491.

Grand, S. P., Van der Hilst, R. D., & Widiyantoro, S. (1997). High resolution global tomography: a snapshot of convection in the Earth. *Geological Society of America Today*, *7*(4).

Guiraud, R., & Maurin, J. C. (1992). Early Cretaceous rifts of Western and Central Africa: an overview. *Tectonophysics*, *213*(1-2), 153-168.

Gurnis, M., Mitrovica, J. X., Ritsema, J., & van Heijst, H. J. (2000). Constraining mantle density structure using geological evidence of surface uplift rates: The case of the African superplume. *Geochemistry, Geophysics, Geosystems*, *1*(7).

Hansen, S. E., & Nyblade, A. A. (2013). The deep seismic structure of the Ethiopia/Afar hotspot and the African superplume. *Geophysical Journal International*, *194*(1), 118-124.

Hansen, S. E., Nyblade, A. A., Julia, J., Dirks, P. H., & Durrheim, R. J. (2009). Upper-mantle low-velocity zone structure beneath the Kaapvaal craton from S-wave receiver functions. *Geophysical Journal International*, *178*(2), 1021-1027.

Hassan, R., Williams, S., Gurnis, M., & Müller, D. (2020). East African topography and volcanism explained by a single, migrating plume. *Geoscience Frontiers*. doi: 10.1016/j.gsf.2020.01.003

Herceg, M., Artemieva, I. M., & Thybo, H. (2016). Sensitivity analysis of crustal correction for calculation of lithospheric mantle density from gravity data. *Geophysical Journal International*, *204*(2), 687-696.

Herrmann, R. B. (2013). Computer programs in seismology: An evolving tool for instruction and research. *Seismological Research Letters*, *84*(6), 1081-1088.

Herrmann, R. B., & Ammon, C. J. (2004). Surface waves, receiver functions and crustal structure. *Computer programs in seismology, version*, *3*, 30.

Hilton, D. R., Halldórsson, S. A., Barry, P. H., Fischer, T. P., de Moor, J. M., Ramirez, C. J., ... & Scarsi, P. (2011). Helium isotopes at Rungwe Volcanic Province, Tanzania, and the origin of East African plateaux. *Geophysical Research Letters*, *38*(21).

Hopper, E., Gaherty, J. B., Shillington, D. J., Accardo, N. J., Nyblade, A. A., Holtzman, B. K., ... & Mulibo, G. D. (2020). Preferential localized thinning of lithospheric mantle in the melt-poor Malawi Rift. *Nature Geoscience*, 1-6.

Huang, Z., Wang, P., Zhao, D., Wang, L., & Xu, M. (2014). Three-dimensional P wave azimuthal anisotropy in the lithosphere beneath China. *Journal of Geophysical Research: Solid Earth*, *119*(7), 5686-5712.

Humphreys, E., & Clayton, R. W. (1988). Adaptation of back projection tomography to seismic travel time problems. *Journal of Geophysical Research: Solid Earth*, *93*(B2), 1073-1085.

Inoue, H., Fukao, Y., Tanabe, K., & Ogata, Y. (1990). Whole mantle P-wave travel time tomography. *Physics of the Earth and Planetary Interiors*, *59*(4), 294-328.

Jackson, J., & Blenkinsop, T. (1993). The Malaŵi earthquake of March 10, 1989: Deep faulting within the East African rift system. *Tectonics*, *12*(5), 1131-1139.

Jelsma, H. A., & Dirks, P. H. (2002). Neoarchaean tectonic evolution of the Zimbabwe Craton. *Geological Society, London, Special Publications*, *199*(1), 183-211.

Johnson, M. R., Anhauesser, C. R., & Thomas, R. J. (2006). The Geology of South Africa. Geological Society of South Africa.

Jones, C. H., Mahan, K. H., Butcher, L. A., Levandowski, W. B., & Farmer, G. L. (2015). Continental uplift through crustal hydration. Geology, 43(4), 355–358. https://doi.org/10.1130/G36509.1

Kachingwe, M., Nyblade, A., & Julia, J. (2015). Crustal structure of Precambrian terranes in the southern African subcontinent with implications for secular variation in crustal genesis. Geophysical Journal International, 202(1), 533-547.

Kadima, E., Delvaux, D., Sebagenzi, S. N., Tack, L., & Kabeya, S. M. (2011). Structure and geological history of the Congo Basin: an integrated interpretation of gravity, magnetic and reflection seismic data. *Basin Research*, *23*(5), 499-527.

Kanamori, H., & Anderson, D. L. (1977). Importance of physical dispersion in surface wave and free oscillation problems. *Reviews of Geophysics*, *15*(1), 105-112.

Kästle, E. D., El-Sharkawy, A., Boschi, L., Meier, T., Rosenberg, C., Bellahsen, N., ... & Weidle, C. (2018). Surface wave tomography of the Alps using ambient-noise and earthquake phase velocity measurements. *Journal of Geophysical Research: Solid Earth*, *123*(2), 1770-1792.

Kästle, E. D., Soomro, R., Weemstra, C., Boschi, L., & Meier, T. (2016). Two-receiver measurements of phase velocity: cross-validation of ambient-noise and earthquake-based observations. *Geophysical Journal International*, *207*(3), 1493-1512.

Kaviani, A., Paul, A., Moradi, A., Mai, P. M., Pilia, S., Boschi, L., ... & Sandvol, E. (2020). Crustal and uppermost mantle shear wave velocity structure beneath the Middle East from surface wave tomography. *Geophysical Journal International*, *221*(2), 1349-1365.

Kennett, B. L. N., Sambridge, M. S., & Williamson, P. R. (1988). Subspace methods for large inverse problems with multiple parameter classes. *Geophysical Journal International*, *94*(2), 237-247.

Kennett, B. L., Engdahl, E. R., & Buland, R. (1995). Constraints on seismic velocities in the Earth from traveltimes. Geophysical Journal International, 122(1), 108-124.

Kennett, B. L. N., Salmon, M., Saygin, E., & Group, A. W. (2011). AusMoho: the variation of Moho depth in Australia. Geophysical Journal International, 187(2), 946-958.

Kgaswane, E. M., Nyblade, A. A., Julià, J., Dirks, P. H., Durrheim, R. J., & Pasyanos, M. E. (2009). Shear wave velocity structure of the lower crust in southern Africa: Evidence for compositional heterogeneity within Archaean and Proterozoic terrains. *Journal of Geophysical Research: solid earth*, *114*(B12).

Kieffer, B., Arndt, N., Lapierre, H., Bastien, F., Bosch, D., Pecher, A., ... & Keller, F. (2004). Flood and shield basalts from Ethiopia: magmas from the African superswell. *Journal of Petrology*, *45*(4), 793-834.

Kind, R., Yuan, X., Saul, J., Nelson, D., Sobolev, S. V., Mechie, J., ... & Jiang, M. (2002). Seismic images of crust and upper mantle beneath Tibet: evidence for Eurasian plate subduction. *science*, *298*(5596), 1219-1221.

King, S. D. (2007). Hotspots and edge-driven convection. *Geology*, *35*(3), 223-226.

King, S. D., & Anderson, D. L. (1995). An alternative mechanism of flood basalt formation. *Earth and Planetary Science Letters*, *136*(3-4), 269-279.

King, S. D., & Anderson, D. L. (1998). Edge-driven convection. *Earth and Planetary Science Letters*, *160*(3-4), 289-296.

King, S. D., & Ritsema, J. (2000). African hot spot volcanism: small-scale convection in the upper mantle beneath cratons. *Science*, *290*(5494), 1137-1140.

Kramers, J. D., S. McCourt, and D. D. van Reenen (2006), The Limpopo Belt, in The Geology of South Africa, edited by M. R. Johnson, C. R. Anhaeusser, and R. J. Thomas, pp. 209 – 236, Geol. Soc. of S. Afr., Johannesburg, South Africa.

Kusky, T. M., Windley, B. F., & Zhai, M. G. (2007). Lithospheric thinning in eastern Asia; constraints, evolution, and tests of models. *Geological Society, London, Special Publications*, *280*(1), 331-343.

Laó-Dávila, D. A., Al-Salmi, H. S., Abdelsalam, M. G., & Atekwana, E. A. (2015). Hierarchical segmentation of the Malawi Rift: The influence of inherited lithospheric heterogeneity and kinematics in the evolution of continental rifts. *Tectonics*, *34*(12), 2399-2417.

Laske, G. & Masters, G. (1997). A Global Digital Map of Sediment Thickness, *EOS Trans. AGU*, 78, F483.

Laske, G., Masters, G., Ma, Z., & Pasyanos, M. (2013). Update on CRUST1. 0—A 1-degree global model of Earth's crust. In *Geophys. Res. Abstr* (Vol. 15, p. 2658).

Lavayssière, A., Rychert, C., Harmon, N., Keir, D., Hammond, J. O., Kendall, J. M., ... & Leroy, S. (2018). Imaging lithospheric discontinuities beneath the Northern East African Rift using S-to-P receiver functions. *Geochemistry, Geophysics, Geosystems*, *19*(10), 4048-4062.

Lebedev, S., Boonen, J., & Trampert, J. (2009). Seismic structure of Precambrian lithosphere: new constraints from broad-band surface-wave dispersion. *Lithos*, *109*(1-2), 96-111.

Legendre, C., Zhao, L., & Chen, Q.-f. (2015). Upper-mantle shear-wave structure under East and Southeast Asia from Automated Multimode Inversion of Waveforms, *Geophysical Journal International*, 203, 707-719.

Lekić, V., Panning, M., & Romanowicz, B. (2010). A simple method for improving crustal corrections in waveform tomography. *Geophysical Journal International*, *182*(1), 265-278.

Lévěque, J. J., Rivera, L., & Wittlinger, G. (1993). On the use of the checker-board test to assess the resolution of tomographic inversions. *Geophysical Journal International*, *115*(1), 313-318.

Li, H., Su, W., Wang, C. Y., & Huang, Z. (2009). Ambient noise Rayleigh wave tomography in western Sichuan and eastern Tibet. *Earth and Planetary Science Letters*, *282*(1-4), 201-211.

Liégeois, J., Benhallou, A., Azzouni-Sekkal, A., Yahiaoui, R., & Bonin, B. (2005). The Hoggar swell and volcanism: reactivation of the Precambrian Tuareg shield during Alpine convergence and West African Cenozoic volcanism. *SPECIAL PAPERS-GEOLOGICAL SOCIETY OF AMERICA*, *388*, 379.

Liégeois, J.-P., Abdelsalam, M. G., Ennih, N., & Ouabadi, A. (2013). Metacraton: Nature, genesis and behavior. *Gondwana Research*, 23(1), 220–237. https://doi.org/10.1016/j.gr.2012.02.016

Lin, F. C., Moschetti, M. P., & Ritzwoller, M. H. (2008). Surface wave tomography of the western United States from ambient seismic noise: Rayleigh and Love wave phase velocity maps. *Geophysical Journal International*, *173*(1), 281-298.

Lithgow-Bertelloni, C., & Silver, P. G. (1998). Dynamic topography, plate driving forces and the African superswell. *Nature*, *395*(6699), 269-272.

Lu, Y., Stehly, L., Paul, A., & AlpArray Working Group. (2018). High-resolution surface wave tomography of the European crust and uppermost mantle from ambient seismic noise. *Geophysical Journal International*, *214*(2), 1136-1150.

Lucassen, F., Franz, G., Romer, R. L., & Dulski, P. (2008). Late Cenozoic xenoliths as a guide to the chemical–isotopic composition and thermal state of the upper mantle under northeast Africa. *European Journal of Mineralogy*, *20*(6), 1079-1096.

Luo, Y., Yang, Y., Xu, Y., Xu, H., Zhao, K., & Wang, K. (2015). On the limitations of interstation distances in ambient noise tomography. *Geophysical Journal International*, *201*(2), 652-661.

Ma, Z., & Masters, G. (2014). A new global Rayleigh-and Love-wave group velocity dataset for constraining lithosphere properties. *Bulletin of the Seismological Society of America*, *104*(4), 2007-2026.

MacGregor, L. M., Constable, S., & Sinha, M. C. (1998). The RAMESSES experiment—III. Controlled-source electromagnetic sounding of the Reykjanes Ridge at 57° 45′ N. *Geophysical Journal International*, *135*(3), 773-789.

Maluski, H., Coulon, C., POPOFF, M. T., & Baudin, P. (1995). 40Ar/39Ar chronology, petrology and geodynamic setting of Mesozoic to early Cenozoic magmatism from the Benue Trough, Nigeria. *Journal of the Geological Society*, *152*(2), 311-326.

Manu-Marfo, D., Aoudia, A., Pachhai, S., & Kherchouche, R. (2019). 3D shear wave velocity model of the crust and uppermost mantle beneath the Tyrrhenian basin and margins. *Scientific reports*, *9*(1), 1-10.

Manya, S., & Maboko, M. A. (2003). Dating basaltic volcanism in the Neoarchaean Sukumaland Greenstone Belt of the Tanzania Craton using the Sm–Nd method: implications for the geological evolution of the Tanzania Craton. *Precambrian Research*, *121*(1-2), 35-45.

McClusky, S., Reilinger, R., Mahmoud, S., Ben Sari, D., & Tealeb, A. (2003). GPS constraints on Africa (Nubia) and Arabia plate motions. *Geophysical Journal International*, *155*(1), 126-138.

McConnell, R. B. (1972). Geological development of the rift system of eastern Africa. *Geological Society of America Bulletin*, *83*(9), 2549-2572.

McCourt, S., & Armstrong, R. A. (1998). SHRIMP U-Pb zircon geochronology of granites from the Central Zone, Limpopo Belt, southern Africa: Implications for the age of the Limpopo Orogeny. *South African Journal of Geology*, *101*(4), 329-338.

Meier, U., Curtis, A., & Trampert, J. (2007). Global crustal thickness from neural network inversion of surface wave data. *Geophysical Journal International*, *169*(2), 706-722.

Milesi, J. P., Frizon de Lamotte, D., de Kock, G., and Toteu, F. (2010). Tectonic Map of Africa, 2nd Edition, Commission for the Geological Map of the World.

Montagner, J. P., Marty, B., Stutzmann, E., Sicilia, D., Cara, M., Pik, R., ... & Debayle, E. (2007). Mantle upwellings and convective instabilities revealed by seismic tomography and helium isotope geochemistry beneath eastern Africa. *Geophysical Research Letters*, *34*(21).

Mooney, W. D., Laske, G., & Masters, T. G. (1998). CRUST 5.1: A global crustal model at 5× 5. *Journal of Geophysical Research: Solid Earth*, *103*(B1), 727-747.

Moschetti, M. P., Ritzwoller, M. H., Lin, F. C., & Yang, Y. (2010). Crustal shear wave velocity structure of the western United States inferred from ambient seismic noise and earthquake data. *Journal of Geophysical Research: Solid Earth*, *115*(B10).

Moulik, P., & Ekström, G. (2014). An anisotropic shear velocity model of the Earth's mantle using normal modes, body waves, surface waves and long-period waveforms. *Geophysical Journal International*, *199*(3), 1713-1738.

Mulibo, G. D., & Nyblade, A. A. (2013). Mantle transition zone thinning beneath eastern Africa: Evidence for a whole-mantle superplume structure. *Geophysical Research Letters*, *40*(14), 3562-3566.

Nataf, H. C., & Ricard, Y. (1996). 3SMAC: an a priori tomographic model of the upper mantle based on geophysical modeling. *Physics of the Earth and Planetary Interiors*, *95*(1-2), 101-122.

Nicollet, C. (1990). Occurrences of grandidierite, serendibite and tourmaline near Ihosy, southern Madagascar. *Mineralogical Magazine*, *54*(374), 131-133.

Niu, F., & James, D. E. (2002). Fine structure of the lowermost crust beneath the Kaapvaal craton and its implications for crustal formation and evolution. *Earth and Planetary Science Letters*, 200(1-2), 121-130.

Nocquet, J. M., & Calais, E. (2003). Crustal velocity field of western Europe from permanent GPS array solutions, 1996–2001. *Geophysical Journal International*, *154*(1), 72-88.

Nyblade, A. A., & Robinson, S. W. (1994). The african superswell. *Geophysical research letters*, *21*(9), 765-768.

Nyblade, A. A., Owens, T. J., Gurrola, H., Ritsema, J., & Langston, C. A. (2000). Seismic evidence for a deep upper mantle thermal anomaly beneath east Africa. *Geology*, *28*(7), 599-602.

Nyblade, A., Dirks, P., Durrheim, R., Webb, S., Jones, M., et al. (2008). AfricaArray: Developing a geosciences workforce for Africa's natural resource sector. *The Leading Edge*, 27(10), 1358-1361.

O'Donnell, J. P., Adams, A., Nyblade, A. A., Mulibo, G. D., & Tugume, F. (2013). The uppermost mantle shear wave velocity structure of eastern Africa from Rayleigh wave tomography: Constraints on rift evolution. *Geophysical Journal International*, *194*(2), 961-978.

Ojo, A. O., Ni, S., & Li, Z. (2017). Crustal radial anisotropy beneath Cameroon from ambient noise tomography. *Tectonophysics*, *696*, 37-51.

Ojo, A. O., Ni, S., Chen, H., & Xie, J. (2018). Crust-mantle coupling mechanism in Cameroon, West Africa, revealed by 3D S-wave velocity and azimuthal anisotropy. *Physics of the Earth and Planetary Interiors*, *274*, 195-213.

Ojo, A. O., Ni, S., Xie, J., & Zhao, L. (2019). Further constraints on the shear wave velocity structure of Cameroon from joint inversion of receiver function, Rayleigh wave dispersion and ellipticity measurements. *Geophysical Journal International*, *217*(1), 589-619.

Owens, T. J., Crotwell, H. P., Groves, C., & Oliver-Paul, P. (2004). SOD: Standing order for data. Seismological Research Letters, 75(4), 515-520.

Panning, M. P., Lekić, V., & Romanowicz, B. A. (2010). Importance of crustal corrections in the development of a new global model of radial anisotropy. *Journal of Geophysical Research: Solid Earth*, *115*(B12).

Park, Y., & Nyblade, A. A. (2006). P-wave tomography reveals a westward dipping low velocity zone beneath the Kenya Rift. *Geophysical Research Letters*, *33*(7).

Pasyanos, M. E., & Nyblade, A. A. (2007). A top to bottom lithospheric study of Africa and Arabia. *Tectonophysics*, *444*(1-4), 27-44.

Pasyanos, M. E., Masters, T. G., Laske, G., & Ma, Z. (2014). LITHO1. 0: An updated crust and lithospheric model of the Earth. *Journal of Geophysical Research: Solid Earth*, *119*(3), 2153-2173.

Petters, S. W. (1991). *Regional geology of Africa* (Vol. 722). Berlin-Heidelberg: Springer-Verlag.

Pik, R., Marty, B., & Hilton, D. R. (2006). How many mantle plumes in Africa? The geochemical point of view. *Chemical Geology*, *226*(3-4), 100-114.

Piqué, A. (1999). The geological evolution of Madagascar: an introduction. *Journal of African Earth Sciences*, *4*(28), 919-930.

Pourpoint, M., Anandakrishnan, S., Ammon, C. J., & Alley, R. B. (2018). Lithospheric structure of Greenland from ambient noise and earthquake surface wave tomography. *Journal of Geophysical Research: Solid Earth*, *123*(9), 7850-7876.

Pratt, M. J., Wysession, M. E., Aleqabi, G., Wiens, D. A., Nyblade, A. A., Shore, P., ... & Barruol, G. (2017). Shear velocity structure of the crust and upper mantle of Madagascar derived from surface wave tomography. *Earth and Planetary Science Letters*, *458*, 405-417.

Priestley, K., McKenzie, D., Debayle, E., & Pilidou, S. (2008). The African upper mantle and its relationship to tectonics and surface geology. *Geophysical Journal International*, *175*(3), 1108-1126.

Rabinowitz, P. D., Coffin, M. F., & Falvey, D. (1983). The separation of Madagascar and Africa. *Science*, *220*(4592), 67-69.

Rawlinson, N., & Sambridge, M. (2004). Multiple reflection and transmission phases in complex layered media using a multistage fast marching method. *Geophysics*, *69*(5), 1338-1350.

Rawlinson, N., & Sambridge, M. (2005). The fast marching method: an effective tool for tomographic imaging and tracking multiple phases in complex layered media. *Exploration Geophysics*, *36*(4), 341-350.

Rawlinson, N., & Spakman, W. (2016). On the use of sensitivity tests in seismic tomography. *Geophysical Journal International*, *205*(2), 1221-1243.

Rawlinson, N., Hauser, J., & Sambridge, M. (2008). Seismic ray tracing and wavefront tracking in laterally heterogeneous media. *Advances in Geophysics*, *49*, 203-273.

Rawlinson, N., Kool, M. D., & Sambridge, M. (2006). Seismic wavefront tracking in 3D heterogeneous media: applications with multiple data classes. *Exploration Geophysics*, *37*(4), 322-330.

Rawlinson, N., Pozgay, S., & Fishwick, S. (2010). Seismic tomography: a window into deep Earth. *Physics of the Earth and Planetary Interiors*, *178*(3-4), 101-135.

Rey, P., Vanderhaeghe, O., & Teyssier, C. (2001). Gravitational collapse of the continental crust: definition, regimes and modes. *Tectonophysics*, 342(3-4), 435-449.

Ring, U. (1994). The influence of preexisting structure on the evolution of the Cenozoic Malawi rift (East African rift system). *Tectonics*, *13*(2), 313-326.

Ritsema, J., & van Heijst, H. (2000). New seismic model of the upper mantle beneath Africa. *Geology*, *28*(1), 63-66.

Ritsema, J., Nyblade, A. A., Owens, T. J., Langston, C. A., & VanDecar, J. C. (1998). Upper mantle seismic velocity structure beneath Tanzania, east Africa: Implications for the stability of cratonic lithosphere. *Journal of Geophysical Research: Solid Earth*, *103*(B9), 21201-21213.

Ritsema, J., van Heijst, H. J., & Woodhouse, J. H. (1999). Complex shear wave velocity structure imaged beneath Africa and Iceland. *Science*, *286*(5446), 1925-1928.

Ritzwoller, M. H., & Levshin, A. L. (1998). Eurasian surface wave tomography: Group velocities. *Journal of Geophysical Research: Solid Earth*, *103*(B3), 4839-4878.

Ritzwoller, M. H., Shapiro, N. M., Barmin, M. P., & Levshin, A. L. (2002). Global surface wave diffraction tomography. *Journal of Geophysical Research: Solid Earth*, *107*(B12), ESE-4.

Rogers, N., Macdonald, R., Fitton, J. G., George, R., Smith, M., & Barreiro, B. (2000). Two mantle plumes beneath the East African rift system: Sr, Nd and Pb isotope evidence from Kenya Rift basalts. *Earth and Planetary Science Letters*, *176*(3-4), 387-400.

Rosenbaum, G., & Lister, G. S. (2004). Neogene and Quaternary rollback evolution of the Tyrrhenian Sea, the Apennines, and the Sicilian Maghrebides. *Tectonics*, *23*(1).

Rozendaal, A., Philander, C., & De Meijer, R. J. (1999). Mineralogy of heavy mineral placers along the west coast of South Africa. In *Heavy Minerals 1999, Symposium S* (Vol. 23, pp. 63-66).

Rudnick, R. L., & Fountain, D. M. (1995). Nature and composition of the continental crust: a lower crustal perspective. *Reviews of geophysics*, 33(3), 267-309.

Rudnick, R. L., & Gao, S. (2003). Composition of the continental crust. The crust, 3, 1-64.

Rychert, C. A., & Shearer, P. M. (2009). A global view of the lithosphere-asthenosphere boundary. *Science*, *324*(5926), 495-498.

Sambridge, M. (1999a). Geophysical inversion with a neighbourhood algorithm—I. Searching a parameter space. *Geophysical journal international*, *138*(2), 479-494.

Sambridge, M. (1999b). Geophysical inversion with a neighbourhood algorithm—II. Appraising the ensemble. *Geophysical Journal International*, *138*(3), 727-746.

Schaeffer, A. J., & Lebedev, S. (2013). Global shear speed structure of the upper mantle and transition zone. *Geophysical Journal International*, *194*(1), 417-449.

Schandelmeier, H., Wipfler, E., Küster, D., Sultan, M., Becker, R., Stern, R. J., & Abdelsalam, M. G. (1994). Atmur-Delgo suture: A Neoproterozoic oceanic basin extending into the interior of northeast Africa. *Geology*, *22*(6), 563-566.

Schlüter, T. (1997). Geology of East Africa.

Schulte-Pelkum, V., Mahan, K. H., Shen, W., & Stachnik, J. C. (2017). The distribution and composition of high-velocity lower crust across the continental US: Comparison of seismic and xenolith data and implications for lithospheric dynamics and history. *Tectonics*, *36*(8), 1455-1496.

Schulte-Pelkum, V., Monsalve, G., Sheehan, A., Pandey, M. R., Sapkota, S., Bilham, R., & Wu, F. (2005). Imaging the Indian subcontinent beneath the Himalaya. *Nature*, *435*(7046), 1222-1225.

Sebai, A., Stutzmann, E., Montagner, J. P., Sicilia, D., & Beucler, E. (2006). Anisotropic structure of the African upper mantle from Rayleigh and Love wave tomography. *Physics of the Earth and Planetary Interiors*, *155*(1-2), 48-62.

Seber, D., Vallvé, M., Sandvol, E., Steer, D., & Barazangi, M. (1997). Middle East tectonics: applications of geographic information systems (GIS). *GSA today*, *7*(2), 1-6.

Selway, K. (2015). Negligible effect of hydrogen content on plate strength in East Africa. *Nature Geoscience*, *8*(7), 543-546.

Sethian, J. A. (1996). A fast marching level set method for monotonically advancing fronts. *Proceedings of the National Academy of Sciences*, *93*(4), 1591-1595.

Sethian, J. A., & Popovici, A. M. (1999). 3-D traveltime computation using the fast marching method. *Geophysics*, *64*(2), 516-523.

Shang, C. K., Satir, M., Morteani, G., & Taubald, H. (2010). Zircon and titanite age evidence for coeval granitization and migmatization of the early Middle and early Late Proterozoic Saharan Metacraton; example from the central North Sudan basement. *Journal of African Earth Sciences*, *57*(5), 492-524.

Shapiro, N. M., & Campillo, M. (2004). Emergence of broadband Rayleigh waves from correlations of the ambient seismic noise. *Geophysical Research Letters*, *31*(7).

Shapiro, N. M., & Ritzwoller, M. H. (2002). Monte-Carlo inversion for a global shear-velocity model of the crust and upper mantle. *Geophysical Journal International*, *151*(1), 88-105.

Shen, W., & Ritzwoller, M. H. (2016). Crustal and uppermost mantle structure beneath the United States. *Journal of Geophysical Research: Solid Earth*, *121*(6), 4306-4342.

Shen, W., Ritzwoller, M. H., & Schulte-Pelkum, V. (2013). A 3-D model of the crust and uppermost mantle beneath the Central and Western US by joint inversion of receiver functions and surface wave dispersion. *Journal of Geophysical Research: Solid Earth*, *118*(1), 262-276.

Simmons, N. A., Forte, A. M., & Grand, S. P. (2007). Thermochemical structure and dynamics of the African superplume. *Geophysical Research Letters*, 34(2).

Simons, F. J., Van Der Hilst, R. D., Montagner, J. P., & Zielhuis, A. (2002). Multimode Rayleigh wave inversion for heterogeneity and azimuthal anisotropy of the Australian upper mantle. *Geophysical Journal International*, *151*(3), 738-754.

Sobh, M., Ebbing, J., Mansi, A. H., Götze, H.-J., Emry, E. L., & Abdelsalam, M. G. (2020). The lithospheric structure of the Saharan Metacraton from 3-D integrated geophysical-petrological modeling. *Journal of Geophysical Research: Solid Earth*, 125, e2019JB018747. https://doi.org/10.1029/2019JB018747

Stankiewicz, J., & de Wit, M. (2013). 3.5 billion years of reshaped Moho, southern Africa. *Tectonophysics*, 609, 675-689.

Storey, M., Mahoney, J. J., Saunders, A. D., Duncan, R. A., Kelley, S. P., & Coffin, M. F. (1995). Timing of hot spot—related volcanism and the breakup of Madagascar and India. *Science*, *267*(5199), 852-855.

Tadjou, J. M., Nouayou, R., Kamguia, J., Kande, H. L., & Manguelle-Dicoum, E. (2009). Gravity Analysis of the Boundary between the Congo Graton and the Pan-African Belt of Cameroon. *Austrian Journal of Earth Sciences*, *102*(1).

Tang, Z., Julià, J., Zahran, H., & Mai, P. M. (2016). The lithospheric shear-wave velocity structure of Saudi Arabia: young volcanism in an old shield. *Tectonophysics*, *680*, 8-27.

Tchameni, R., Mezger, K., Nsifa, N. E., & Pouclet, A. (2001). Crustal origin of Early Proterozoic syenites in the Congo craton (Ntem complex), South Cameroon. *Lithos*, *57*(1), 23-42.

Tedla, G. E., Van Der Meijde, M., Nyblade, A. A., & Van der Meer, F. D. (2011). A crustal thickness map of Africa derived from a global gravity field model using Euler deconvolution. *Geophysical Journal International*, *187*(1), 1-9.

Thomas, R. J. (1989). A tale of two tectonic terranes. *South African Journal of Geology*, *92*(4), 306-321.

Thompson, D. A., Bastow, I. D., Helffrich, G., Kendall, J. M., Wookey, J., Snyder, D. B., & Eaton, D. W. (2010). Precambrian crustal evolution: seismic constraints from the Canadian Shield. *Earth and Planetary Science Letters*, 297(3-4), 655-666.

Thybo, H., Youssof, M., & Artemieva, I. M. (2019). Southern Africa crustal anisotropy reveals coupled crust-mantle evolution for over 2 billion years. *Nature communications*, *10*(1), 1-10.

Tokam, A. P. K., Tabod, C. T., Nyblade, A. A., Julia, J., Wiens, D. A., & Pasyanos, M. E. (2010). Structure of the crust beneath Cameroon, West Africa, from the joint inversion of Rayleigh wave group velocities and receiver functions. *Geophysical Journal International*, *183*(2), 1061-1076.

Torsvik, T. H., Tucker, R. D., Ashwal, L. D., Eide, E. A., Rakotosolofo, N. A., & De Wit, M. J. (1998). Late Cretaceous magmatism in Madagascar: palaeomagnetic evidence for a stationary Marion hotspot. *Earth and Planetary Science Letters*, *164*(1-2), 221-232.

Trampert, J., & Woodhouse, J. H. (1995). Global phase velocity maps of Love and Rayleigh waves between 40 and 150 seconds. *Geophysical Journal International*, *122*(2), 675-690.

Tugume, F., Nyblade, A., & Julià, J. (2012). Moho depths and Poisson's ratios of Precambrian crust in East Africa: evidence for similarities in Archean and Proterozoic crustal structure. *Earth and Planetary Science Letters*, 355, 73-81.

Tugume, F., Nyblade, A., Julià, J., & van der Meijde, M. (2013). Precambrian crustal structure in Africa and Arabia: evidence lacking for secular variation. *Tectonophysics*, *609*, 250-266.

Turner, S., Regelous, M., Kelley, S., Hawkesworth, C., & Mantovani, M. (1994). Magmatism and continental break-up in the South Atlantic: high precision40Ar-39Ar geochronology. *Earth and Planetary Science Letters*, *121*(3-4), 333-348.

Van der Meijde, M., Fadel, I. E. A. M., Ditmar, P., & Hamayun, M. (2015). Uncertainties in crustal thickness models for data sparse environments: A review for South America and Africa. *Journal of Geodynamics*, *84*, 1-18.

Veevers, J. J., Cole, D. I. & Cowan, E. J. (1994). Southern Africa: Karoo Basin and Cape Fold Belt. In: Veevers, J. J. & Powell, C. McA. (eds) *Permian Triassic Pangean Basins and Foldbelts along the Panthalassan Margin of Gondwanaland. Geological Society of America, Memoirs* 184, 223-279.

Vergés, J. & Sàbat, F. (1999) Constraints on the western Mediterranean kinematics evolution along a 1,000 -km transect from Iberia to Africa. In: *The Mediterranean Basins:Tertiary Extension within the Alpine Orogen* (Ed. by B. Durand, L. Jolivet, F. Horvath & M. Se¤ranne), pp. 63^80, Geol. Soc. Spec. Pub., 156

Wang, T., Gao, S. S., Dai, Y., Yang, Q., & Liu, K. H. (2019). Lithospheric Structure and Evolution of Southern Africa: Constraints From Joint Inversion of Rayleigh Wave Dispersion and Receiver Functions. *Geochemistry, Geophysics, Geosystems*, *20*(7), 3311-3327.

Weeraratne, D. S., Forsyth, D. W., Fischer, K. M., & Nyblade, A. A. (2003). Evidence for an upper mantle plume beneath the Tanzanian craton from Rayleigh wave tomography. *Journal of Geophysical Research: Solid Earth*, *108*(B9).

Welford, J. K., Clowes, R. M., Ellis, R. M., Spence, G. D., Asudeh, I., & Hajnal, Z. (2001). Lithospheric structure across the craton-Cordilleran transition of northeastern British Columbia. *Canadian Journal of Earth Sciences*, *38*(8), 1169-1189.

Wessel, P., Smith,W. H. F., Scharroo, R., Luis, J., & Wobbe, F. (2013). Generic mapping tools: Improved version released. *Eos, Transactions American Geophysical Union*, *94*(45), 409–410. https://doi.org/10.1002/2013EO450001

Williams, M. L., Dumond, G., Mahan, K., Regan, S., & Holland, M. (2014). Garnet-forming reactions in felsic orthogneiss: Implications for densification and strengthening of the lower continental crust. *Earth and Planetary Science Letters*, *405*, 207-219.

Wilson, M., and R. Guiraud (1992), Magmatism and rifting in Western and Central Africa, from Late Jurassic to Recent times, Tectonophysics, 213, 203–225.

Wittlinger, G., Farra, V., Hetényi, G., Vergne, J., & Nábělek, J. (2009). Seismic velocities in Southern Tibet lower crust: a receiver function approach for eclogite detection. *Geophysical Journal International*, *177*(3), 1037-1049.

Wolfenden, E., Ebinger, C., Yirgu, G., Deino, A., & Ayalew, D. (2004). Evolution of the northern Main Ethiopian rift: birth of a triple junction. *Earth and Planetary Science Letters*, *224*(1-2), 213-228.

Woodhouse, J. H., & Dziewonski, A. M. (1984). Mapping the upper mantle: Three-dimensional modeling of Earth structure by inversion of seismic waveforms. *Journal of Geophysical Research: Solid Earth*, *89*(B7), 5953-5986.

Xia, Y., & Chen, X. (2020). Observation of a New Long-Period (16-s) Persistent Tremor Originating in the Gulf of Guinea. Geophysical Research Letters, 47(15), e2020GL088137.

Xia, Y., Ni, S., & Zeng, X. (2013). Twin enigmatic microseismic sources in the Gulf of Guinea observed on intercontinental seismic stations. *Geophysical Journal International*, *194*(1), 362-366.

Yang, Y., & Ritzwoller, M. H. (2008). Characteristics of ambient seismic noise as a source for surface wave tomography. *Geochemistry, Geophysics, Geosystems*, *9*(2).

Yang, Y., Ritzwoller, M. H., Levshin, A. L., & Shapiro, N. M. (2007). Ambient noise Rayleigh wave tomography across Europe. *Geophysical Journal International*, *168*(1), 259-274.

Yang, Y., Ritzwoller, M. H., Lin, F. C., Moschetti, M. P., & Shapiro, N. M. (2008a). Structure of the crust and uppermost mantle beneath the western United States revealed by ambient noise and earthquake tomography. *Journal of Geophysical Research: Solid Earth*, *113*(B12).

Yang, Y., Li, A., & Ritzwoller, M. H. (2008b). Crustal and uppermost mantle structure in southern Africa revealed from ambient noise and teleseismic tomography. *Geophysical Journal International*, *174*(1), 235-248.

Yao, H., Beghein, C., & Van Der Hilst, R. D. (2008). Surface wave array tomography in SE Tibet from ambient seismic noise and two-station analysis-II. Crustal and upper-mantle structure. *Geophysical Journal International*, *173*(1), 205-219.

Yao, H., van Der Hilst, R. D., & De Hoop, M. V. (2006). Surface-wave array tomography in SE Tibet from ambient seismic noise and two-station analysis—I. Phase velocity maps. *Geophysical Journal International*, *166*(2), 732-744.

Yao, H., Van Der Hilst, R. D., & Montagner, J. P. (2010). Heterogeneity and anisotropy of the lithosphere of SE Tibet from surface wave array tomography. *Journal of Geophysical Research: Solid Earth*, *115*(B12).

Yao, Z., Mooney, W. D., Zahran, H. M., & Youssef, S. E. H. (2017). Upper mantle velocity structure beneath the Arabian shield from Rayleigh surface wave tomography and its implications. *Journal of Geophysical Research: Solid Earth*, *122*(8), 6552-6568.

Yoshizawa, K., & Ekström, G. (2010). Automated multimode phase speed measurements for high-resolution regional-scale tomography: application to North America. *Geophysical Journal International*, *183*(3), 1538-1558.

Youssof, M., Thybo, H., Artemieva, I. M., & Levander, A. (2013). Moho depth and crustal composition in Southern Africa. *Tectonophysics*, *609*, 267-287.

Zandt, G., Gilbert, H., Owens, T. J., Ducea, M., Saleeby, J., & Jones, C. H. (2004). Active foundering of a continental arc root beneath the southern Sierra Nevada in California. *Nature*, 431(7004), 41-46.

Zeng, X., & Ni, S. (2011). Correction to A persistent localized microseismic source near the Kyushu Island, Japan. *Geophysical Research Letters*, *38*(16).

Zhao, D. (2015). *Multiscale seismic tomography*. Springer.

Zhou, L., Xie, J., Shen, W., Zheng, Y., Yang, Y., Shi, H., & Ritzwoller, M. H. (2012). The structure of the crust and uppermost mantle beneath South China from ambient noise and earthquake tomography. *Geophysical Journal International*, *189*(3), 1565-1583.

Zhou, Y., Nolet, G., Dahlen, F. A., & Laske, G. (2006). Global upper-mantle structure from finite-frequency surface-wave tomography. *Journal of Geophysical Research: Solid Earth*, *111*(B4).

1466